X-RAY SPECTRAL ANALYSIS OF THE STEADY STATES OF GRS1915+105

The Astrophysical Journal, 822:60 (19pp), 2016 May 10 doi:10.3847/0004-637X/822/2/60

X-RAY SPECTRAL ANALYSIS OF THE STEADY STATES OF GRS1915+105

Charith S. Peris[1,2], Ronald A. Remillard[3], James F. Steiner[1,3], Saeqa D. Vrtilek[1], Peggy Varnière[4], Jerome Rodriguez[5], and Guy Pooley[6]
[1] Harvard-Smithsonian Center for Astrophysics, 60 Garden Street, Cambridge, MA 02138, USA; cperis@cfa.harvard.edu
[2] Department of Physics, Northeastern University, 360 Huntington Avenue, Boston, MA 02115, USA
[3] Kavli Institute for Astrophysics and Space Research, MIT, Cambridge, MA 02139, USA
[4] APC, AstroParticule & Cosmologie, UMR 7164 CNRS/N2P3, Université Paris Diderot, CEA/Irfu, Observatoire de Paris, Sorbonne Paris Cité, 10 rue Alice Domon et Léonie Duquet, F-75205 Paris Cedex 13, France
[5] Laboratoire AIM, CEA/IRFU-CNRS/INSU-Université Paris Diderot, CEA DSM/IRFU/SAp, Centre de Saclay, F-91191 Gif-sur-Yvette, France
[6] Astrophysics, Cavendish Laboratory, Madingley Road, Cambridge CB3 0HE, UK
Received 2015 September 28; accepted 2016 February 28; published 2016 May 5

ABSTRACT

We report on the X-ray spectral behavior within the steady states of GRS1915+105. Our work is based on the full data set of the source obtained using the Proportional Counter Array (PCA) on the *Rossi X-ray Timing Explorer* (*RXTE*) and 15 GHz radio data obtained using the Ryle Telescope. The steady observations within the X-ray data set naturally separated into two regions in the color–color diagram and we refer to these regions as steady-soft and steady-hard. GRS1915+105 displays significant curvature in the coronal component in both the soft and hard data within the *RXTE*/PCA bandpass. A majority of the steady-soft observations displays a roughly constant inner disk radius ($R_{\rm in}$), while the steady-hard observations display an evolving disk truncation which is correlated to the mass accretion rate through the disk. The disk flux and coronal flux are strongly correlated in steady-hard observations and very weakly correlated in the steady-soft observations. Within the steady-hard observations, we observe two particular circumstances when there are correlations between the coronal X-ray flux and the radio flux with log slopes $\eta \sim 0.68 \pm 0.35$ and $\eta \sim 1.12 \pm 0.13$. They are consistent with the upper and lower tracks of Gallo et al. (2012), respectively. A comparison of the model parameters to the state definitions shows that almost all of the steady-soft observations match the criteria of either a thermal or steep power-law state, while a large portion of the steady-hard observations match the hard-state criteria when the disk fraction constraint is neglected.

Key words: accretion, accretion disks – binaries: close – black hole physics – magnetic fields – X-rays: binaries – X-rays: individual (GRS1915+105)

Supporting material: machine-readable table

1. INTRODUCTION

The primary source of information about stellar-mass black holes in the Milky way and nearby galaxies is the radiation from mass accretion systems known as black hole binaries (BHBs). These systems consist of a secondary donor star that transfers matter onto the black hole, creating an X-ray luminous accretion disk. Today, we have >20 binary systems, which have a dynamically determined primary mass above 3 $M_{\odot}$: this is strong evidence supporting the presence of a black hole.

The X-ray spectra of most BHBs are readily describable using a simple model consisting of a multi-temperature accretion disk component together with a hard X-ray power-law component which is widely attributed to inverse-Compton scattering of disk photons in a hot corona and modeled using a simple power-law or cutoff power-law function (McClintock & Remillard 2006, pp. 157–213). In most cases, an Fe Kα emission line should be included at ~6.4 keV. Sometimes it is necessary to add a disk reflection component when the inclination angle is $\leqslant 60°$. In some cases, absorption features are also evident (Ueda et al. 1998, see also Sobczak et al. 2000). Broadly speaking, this class of models has been employed to satisfactorily fit many spectra of numerous BHBs (e.g., LMC X-1, LMC X-3, GX339-4, Ebisawa 1991; GS 2000+25, Ebisawa 1991; Takizawa 1991; Terada et al. 2002; GS 1354-64, Kitamoto et al. 1990; and Nova Muscae 91, Ebisawa et al. 1994; GRO J1650-40, Sobczak et al. 1999; XTE J1550-564, Sobczak et al. 2000) and has been an essential tool in forming a physical picture of these sources. Such endeavors at spectral fitting via such simple modeling have revealed that while individual BHBs have their own behavioral tendencies, BHBs generally occupy a few distinctive X-ray spectral-timing states (e.g., Fender & Belloni 2004; Remillard & McClintock 2006 hereafter RM06).

A black hole in outburst typically occupies one of three states: the thermal state, the hard state, or the steep power-law state (SPL; RM06). Loosely defined, the thermal state (also called the high/soft state) features domination of the X-ray spectrum by a hot accretion disk. The hard state (or low/hard state) features domination by a hard X-ray corona that is related to a steady radio jet. The SPL state (sometimes referred to as the very high state) shows a significant contribution from a steep power-law component that is linked to activity in a hot corona, the absence of a steady jet, but the possible production of a transient jet and a prominent disk. These states have been pivotal in understanding the physics that generates different modes of black hole accretion.

Of the BHBs discovered thus far, GRS1915+105 (hereafter referred to as GRS1915) stands out as exceptional in many ways. It was discovered in 1992 by the WATCH all-sky monitor on board *GRANAT* as a transient Galactic source (Castro-Tirado et al. 1992) and it sparked a great deal of interest as the first Galactic object discovered to exhibit superluminal motion in its radio jets (Mirabel & Rodríguez 1994; Fender et al. 1999b). These Galactic radio jet sources, which display bipolar radio emission analogous to that

observed in radio-loud active galactic nuclei (AGNs), are known as "microquasars". Initial estimates suggested a $\sim 14 M_{\odot}$ black hole (Greiner et al. 2001). More recently, a trigonometric parallax was measured for the radio nucleus yielding a distance of $8.6^{+2.0}_{-1.6}$ kpc and a revised primary mass of $12.4^{+2.0}_{-1.8}\,M_{\odot}$ (Reid et al. 2014). Using a quantitative definition of the thermal state, McClintock et al. (2006) selected 22 disk-dominated observations and calculated its spin to be $a_{*} > 0.98$, establishing GRS1915 as an extreme Kerr-hole.

Among the fundamental characteristics that set this black hole apart from the rest is GRS1915's wild X-ray variability, the diversity of which has not been replicated in any other stellar-mass black hole. The complex X-ray light curves of GRS1915 span at least 14 different variability classes (Belloni et al. 2000; Klein-Wolt et al. 2002; Hannikainen et al. 2005) and were thought to be unique until the recent discovery of a few similar patterns in IGR J17091-3624 (Altamirano et al. 2011). However, even though extreme variability is commonplace in its light curve, about half of the observations of GRS1915 show fairly steady X-ray intensity (see Section 2.1), and most of these intervals yield spectra and power density spectra (PDS) that seem to resemble one of the three states (see Section 5; see also Muno et al. 1999; Klein-Wolt et al. 2002; McClintock & Remillard 2006, pp. 157–213). This suggests that within the complexity of this source is a simpler underlying basis of states which may map to those observed in canonical BHBs.

Historically, X-ray spectral analyses of the hot inner accretion disks in thermal states have shown that as the flux varies by several orders of magnitude, the value of the inner disk radius ($R_{\rm in}$) remains remarkably constant (Tanaka & Lewin 1995, p. 126). This is also true for SPL state observations with low or modest Compton scattering fractions (Steiner et al. 2009a). The stability of $R_{\rm in}$ suggests a relationship with the innermost stable circular orbit ($R_{\rm ISCO}$), as prescribed by General Relativity. In the hard and quiescent states, however, direct measurements of the thermal emission from the inner disk have been elusive. The low temperatures of hard-state disks makes them nearly undetectable for many instruments (e.g., XTE J1118+480, ~0.024 keV, McClintock et al. 2001; Swift J1753.5-0127, ~0.2 keV, Miller et al. 2006, ~0.28–0.37 keV, Miller & Rykoff 2007; GX339-4, ~0.24 keV, Belloni et al. 2013; ~0.22 keV, Shidatsu et al. 2011; Cyg X-1, ~0.2 keV, Makishima et al. 2008). This has led to studies in the hard state being focused primarily on the power-law component of the spectrum using the observed flux as an approximation to the total coronal flux. In this context, GRS1915 presents a unique opportunity. It displays a consistently hot disk even in its harder states (Muno et al. 1999). We will also exploit this high-temperature disk to separate out the disk and coronal contributions to the spectrum and explore their behavior within both soft and hard observations.

Correlations between the radio and X-ray fluxes of hard- and quiescent-state BHBs have been a source of interest as they indicate a likely physical relationship between the radio jet and the X-ray emitting corona (and possibly the disk as well). After Corbel et al. (2003) first reported the correlation over a wide flux range for GX339-4, Gallo et al. (2003, 2006) found that the same relationship ($L_r \propto L_{\rm X}^{\eta}$ where $\eta = 0.58 \pm 0.16$) held for a number of hard-state black holes. Gallo et al. (2012) revisited this inquiry and critically investigated a growing number of outliers to the X-ray–radio correlation, finding evidence for a distinct second track (see also Coriat et al. 2011). The first track of $\eta = 0.63 \pm 0.03$ corresponded to the prior track and a second track was revealed with log slope $\eta = 0.98 \pm 0.08$. These two tracks are thought to reflect different accretion regimes within the hard state. Gallo et al. (2012) did not include GRS1915 in their analysis.

The X-ray–radio correlation in GRS1915 was investigated by Rushton et al. (2010) using the Rossi X-ray Timing Explorer (RXTE)/All-Sky Monitor (ASM) and Ryle telescope data. They found close coupling between the mechanisms that produced the X-ray and radio emission within the hard observations displaying a steady radio jet ("radio plateau" states; Muno et al. 2001), which they fitted with an index of $\eta \sim 1.7 \pm 0.3$. This index, which showed GRS1915 to be distinct from other BHBs, suggested that the dominant mode of hard-state accretion in GRS1915 is efficient, unlike canonical BHB hard states. However, the ASM provides only the total flux. We will employ our complete RXTE/Proportional Counter Array (PCA) data set of GRS1915 to revisit and explore the X-ray–radio correlation with the ability to clearly distinguish the coronal flux from the total flux.

The spectrum of GRS1915 has been notoriously difficult to describe using standard BHB models (see Muno et al. 1999; McClintock et al. 2006; Titarchuk & Seifina 2009). Therefore, our main goal is to fit a majority of our data, which consist of an ensemble of locally steady conditions of GRS1915 (described in detail in Section 2.1), with the simplest possible phenomenological models. We will discuss the correlations between the model parameters, which will include addressing simple questions such as the following: How does the inner radius of the accretion disk behave? Does the disk exhibit any connection to the corona? Do the corona and the disk show a connection to the radio jet? We will then attempt to explain the physics revealed by the parameter variation.

In Section 2, we describe our observations. In Section 3, we present an overview of the spectral modeling process terminating with a description of the successful models that we use to analyze the data. We present the results of our spectral analysis in Section 4, followed by a comparison of our observations to canonical BHB states and to the variable states of GRS1915 (Belloni et al. 2000) in Section 5. We discuss the implications of our results in Section 6 and end with a summary of our core conclusions.

2. OBSERVATIONS

2.1. X-Ray Data

RXTE consists of three instruments: the PCA, the High-Energy X-ray Timing Experiment, and the ASM. The *RXTE*/PCA consists of five co-aligned proportional counter units (PCUs), each with a collecting area of $\sim 1600\,{\rm cm}^2$ and a xenon-filled detector volume with three layers of signal anodes. It is sensitive over a range of approximately 2–60 keV with an energy resolution of $\approx 18\%$ at 6 keV (see Jahoda et al. 2006).

The spectral fitting was conducted on data obtained using all of the layers of proportional counter unit 2 (PCU-2) because it was operating during almost every observation. The PCA background subtraction was conducted using the pcabackest task of the HEASOFT/FTOOLS package. We used the composite bright/faint source model of Markwardt (2012).

In this study, the elemental spectra consist of continuous data segments that occur between the common interruptions

imposed by Earth occultations and the passage of the *RXTE* spacecraft through the South Atlantic Anomaly. We further imposed a segment break when the number of PCUs was changed or to exclude data when one of the PCUs was not operating properly.

During its operational period, *RXTE*/PCA observed GRS1915 ~1800 times. We filtered this data for continuous data segments greater than 400 s in both the standard 1 and standard 2 data modes and found 2565 intervals exceeding 5.2 Ms with a mean exposure of 2.1 ks. After imposing the further requirement that PCU-2 spectra be available with standard 2 data, the total number of data segments available was 2563.

We selected four energy bands A (2.2–3.6 keV), B (3.6–5.0 keV), C (5.0–8.6 keV), and D (8.6–18.0 keV) and defined the soft color—or hardness ratio—HR1 as the count rate in B divided by the count rate in A; and the hard color (HR2) as D/C. The four PCA energy bands are used to compute a color–color diagram (CD) and a hardness-intensity diagram (HID), with a scheme to normalize the count rates in each band, throughout the PCA times of observation (1996–2012). Such normalized CDs and HIDs are shown for accreting black holes and neutron stars in Muno et al. (2002), RM06, and Lin et al. (2007). However, there is one significant difference in the normalization strategy used in the present paper. Previously, it was assumed that the X-ray spectrum of the Crab Nebula is invariant, and the PCA count rates in each energy band were normalized to ensure that the Crab CD and HID display constant values, except for statistical fluctuations. However, it has been shown that the Crab Nebula actually varies at the level of several percent over timescales of months (Wilson-Hodge et al. 2011). Their work utilized observations from several instruments, including the *RXTE*/PCA. It can be concluded that the physical model for the PCA Instrument, which is used to normalize the PCA response files, is "stiffer" than the Crab variations, i.e., the model parameters change on longer timescales, allowing us to observe the Crab variations.

In the present investigation, the PCA response files serve as the basis for the 4-band normalizations. We simulated Crab-like spectra (XSPEC: FAKEIT) at 30 day intervals between 1996 January and 2012 January. The simulated spectra adopted the mean PCA Crab spectral parameters, i.e., a power law with photon index (Γ) 2.11, normalization constant 10.55, and interstellar absorption $N_H = 3.45 \times 10^{21}\,\mathrm{cm}^{-2}$. For each simulated PCU spectrum, we extracted the count rates within the four intervals noted above. We then normalized each band to global constants, using piece-wise linear fits during each PCU gain epoch. The targeted normalization constants per energy band are the same as the values used in Lin et al. (2007), i.e., 550, 550, 850, and 570 counts s^{-1}. The normalization parameters per PCU and per time interval can then be applied to any PCA data.

There is one caveat to this process that concerns the lowest energy band (channel A). When the Crab observations themselves are normalized by the response files, via the Crab-simulated spectra described above, the mean values for the normalized energy bands agree with the target values, except for channel A. There is a very significant discrepancy between the real Crab spectra and the simulated spectra at energies below ~3 keV where there are substantial numbers of counts. This discrepancy underlies the common practice of PCA users to adopt lower limits for spectral fitting that are typically in the range ~2.5–3.0 keV. We choose to compensate for this problem by imposing an additional normalization constant per PCU and per gain epoch for channel A (only) that brings the real Crab count rates in line with the target value. The additional correction factors to the A Channel are typically in the range 5%–15%, depending on PCU and time interval. Such values are similar to or less than the factors that normalize different PCUs during a given time interval, or the factors that relate different time epochs for a given PCU (e.g., across the times of gain changes or the times when the propane layer was lost for two of the PCUs).

This paper is focused on the results of spectral fits for the data segments that we infer to be quasi-steady. We have found that the best way to define quasi-steady conditions is to consider three measurement quantities: the source fractional variations (i.e., rms/mean) in 1 s bins, the same measurement in 16 s bins, and the rms variations in the soft color (HR1). Each of these quantities allows us to easily identify the types of variable light curves characterized by high-amplitude cycles that operate at timescales of minutes or longer (e.g., variability classes β, ν, μ, θ, λ, κ, ρ; see Belloni et al. 2000). However, there are overlapping values of fractional variability (e.g., at 1 s) between light curve types that would appear to be quasi-steady (e.g., class χ, which displays hard-state flickering widely treated as quasi-steady), as opposed to others that display tracks in the CD which suggest temperature variations that cannot be averaged (e.g., weaker episodes of classes γ or δ). We report, in advance, that none of the conclusions offered in this paper are changed if we impose additional restrictions that eliminate data selections when weak γ or δ characteristics appear in the light curves. Such cases are subtle and would amount to 1%–2% and 4%–5% of the steady intervals, respectively.

The values displayed by GRS1915 for the three variability quantities are shown in Figure 1. We select segments as "quasi-steady" if the fractional variability at 1 s is less than 0.12, the fractional variability at 16 s is less than 0.08, and the variation in HR1 (16 s) is less than 0.03. These selection criteria are displayed with blue lines in the lower left corner of each panel in Figure 1. There are 1257 data segments (which is 49% of 2563 total) that lie in both selection boxes.

The HID and CD of GRS1915 are displayed in Figure 2 for the 1257 steady observations (2.55 Ms total exposure) which are the focus of this paper. The gaps between these steady observations show a broad distribution, ranging from 0.1 to 35 days (with an average of 2.2 days). We divide these observations into two groups which are best separated in the CD. We refer to the softer extended set of observations as "steady-soft" (red circles; 264 data points totaling 0.54 Ms) and the dense cluster of harder points as "steady-hard" (black squares; 993 data points totaling 2.01 Ms) throughout this paper. A tiny clump of points at [0.4, 1.55] in the CD which appeared ambiguous in the classification was identified as steady-soft, using the low integrated rms power (0.1–10 Hz) to the classification. We note that this soft/hard separation is based only on the location of the observations in the CD and not on the more general thermal state and hard-state classifications given by RM06.

2.2. Simultaneous Radio Data

The Ryle telescope (now transformed into the AMI large array) located at the Mullard Radio Astronomy Observatory in

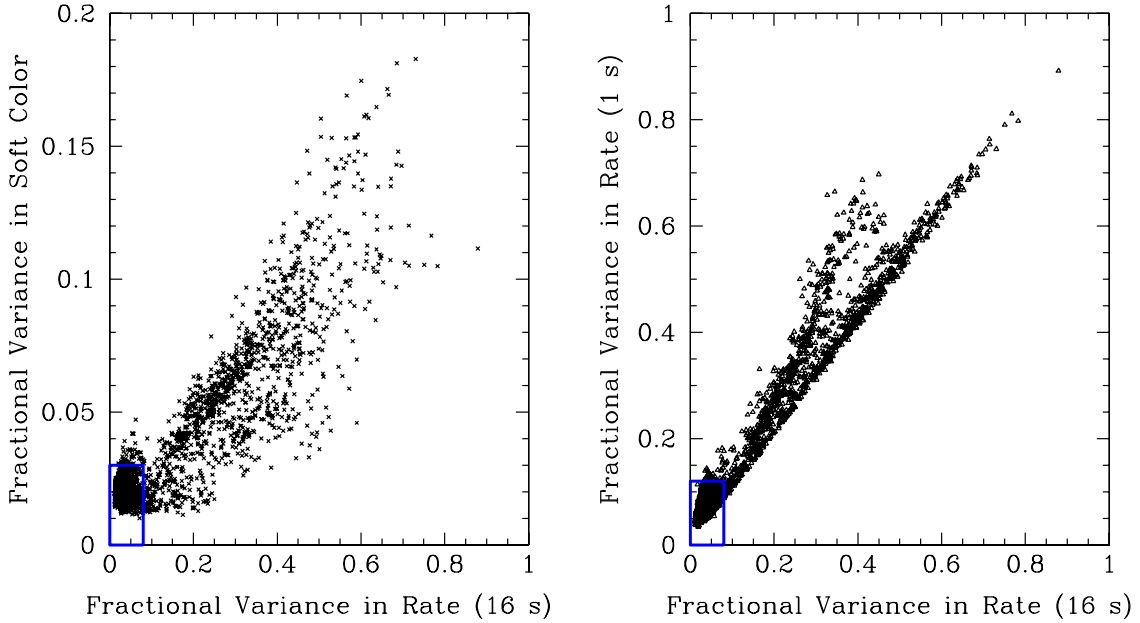

Figure 1. Observations are termed "quasi-steady" if the fractional variability at 1 s is less than 0.12, the fractional variability at 16 s is less than 0.08, and the variation in HR1 (16 s) is less than 0.03. These observations fall within both blue boxes in the plots shown.

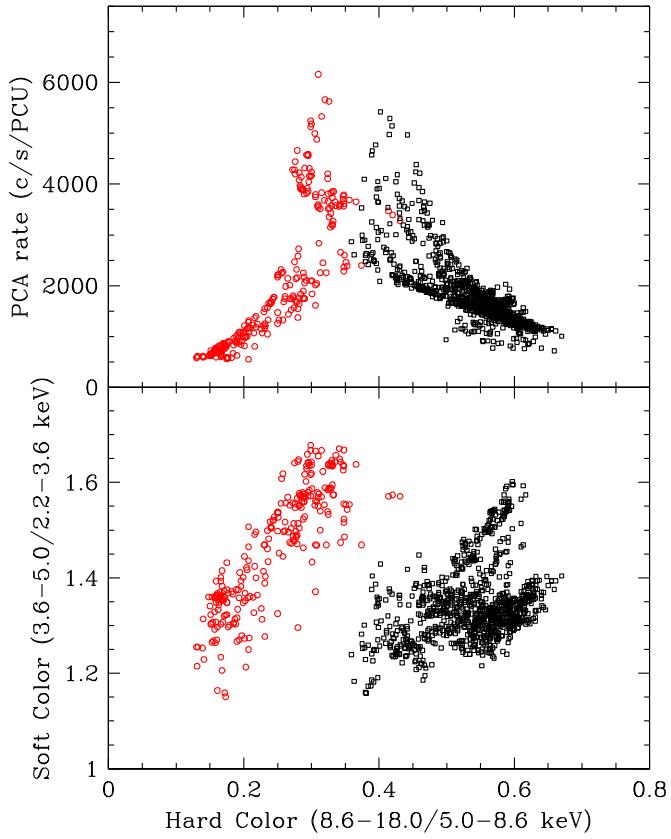

Figure 2. Hardness-intensity diagram (HID; top) and the color–color diagram (CD; bottom) of the steady state data of GRS1915. The steady-soft observations are represented by red circles and the steady-hard observations by black squares.

the UK was an east–west radio interferometer primarily used for microwave-background studies. Its standard observations were 12 hr apiece, so as to fill the synthesized aperture. In order to monitor sources with short-period variability, a program began using interstitial intervals between the standard (long) observations. This program, documented by Pooley & Fender (1997), collected nearly daily observations of GRS1915, at 15 GHz, from 1995 May to 2006 June; providing a 10 year overlap with our *RXTE*/PCA X-ray observations. We used the data from this program to study the radio properties of GRS1915 corresponding to its behavior at X-ray wavelengths.

Although baselines between 18 m and 4.8 km were available in a variety of configurations, most of the data used in this study were obtained using a more compact array, typically less than 150 m. Observations were alternated with a nearby calibrator, B 1920+154, so that the instrumental phase variations could be detected and removed. The flux-density scale was set using 3C 48 and 3C 286. The data were sampled every 8 s and averaged into 5 minute data points with an rms noise of ∼2 mJy (Pooley & Fender 1997; Prat et al. 2010; Rushton et al. 2010). We typically average over a longer time period in our study and our fractional uncertainty is reduced.

To investigate the X-ray–radio correlations, we explored either restrictively analyzing the strictly simultaneous observations or alternatively employing a larger sample for which the observation mid-times matched within ±0.5 days. In each case, we took the mean value of all of the radio data points corresponding to each X-ray observation as the corresponding radio flux of that observation. Since the results in both cases were consistent, we employ the latter selection—which is a significantly larger pool of data—in our full analysis presented below. We found 70 and 624 radio-matched X-ray observations in steady-soft and steady-hard, respectively.

3. SPECTRAL MODELING

In this section, we describe the fitting process and the models employed for the spectral fits. All of the fitting was performed using XSPEC 12.8.1 (Arnaud 1996). Spectra were fit over the energy range 2.52–45 keV. The lower limit of 2.52 keV reflects the low-energy calibration limit of the detector, and the upper value of 45 keV is chosen due to calibration uncertainty and

low effective area at higher energies. To improve the sensitivity of our fits, we used a more recent and improved calibration tool PCACORR (García et al. 2014). While PCACORR comes with a recommended systematic uncertainty as low as 0.1%, we employ the customarily used 1% systematic uncertainty (e.g., Jahoda et al. 2006) for GRS1915 driven by the simplicity of the models we employ.

After using the xspec fit command for the initial fitting, xspec's "error" command was used to find approximate confidence ranges for our main fit parameters. The error command varies the relevant parameter within its hard limits and finds the change in value required to reach $\Delta\chi^2$, which corresponds to the desired confidence interval for 1 degree of freedom and assuming Gaussian statistics. In some cases, as a byproduct of this detailed search for the confidence interval, a new minimum for the fit-statistic may be found.

Given the approximate and idealized nature of the models available to fit the spectra of BHBs, we delineated between successful "good fits" and "poor fits" by adopting a critical goodness-of-fit $\chi^2_\nu < 2$ (see also Steiner et al. 2010, 2011), which is appropriate for *RXTE*/PCA. We use only the "good fits" for all of our analyses. The extremely large number of counts per spectrum in GRS1915 (~5 million) reduce the channel errors significantly. This means that the uncertainty for many measurement bins is dominated by the systematic error, in which case our selection criteria admits errors (when using our simple models) of the order of ~1.4%.

3.1. First Model Attempts

In this section, we describe a subset of the models investigated to find the simplest ones that best fit the majority of the X-ray spectra. Up to 70 different model variants were explored with most producing unsatisfactory results. Typical BHB models incorporate a multi-temperature accretion disk coupled with a standard power-law component (a proxy for inverse-Compton scattering) and an Fe–Kα line component. We found that this simplest construction failed and that a strong requirement was the inclusion of a cutoff (i.e., curvature) with an unusually low folding energy in the power-law component in order to produce good fits. This result established that the Compton component of GRS1915 (hereafter referred to, in a more physical sense, as the "coronal component") is unusually curved within the PCA bandpass. An exponential cutoff was also used in analyses by Muno et al. (1999) and Neilsen et al. (2011).

Gamma-ray observations by Grove et al. (1998) detected emission from GRS1915 at energies up to ~1 MeV. X-ray observations by Zdziarski et al. (2001) and Rodriguez et al. (2008) also confirmed the presence of a power-law-like component at higher energies, in addition to observing curvature in the spectrum consistent with our observations at energies <45 keV. Our fits indicate that an additional power law added into our fits does not affect our χ^2_ν values or the number of good fits. However, an added power law cannot be constrained given the limited bandwidth available using *RXTE*/PCA. Therefore, we do not use it for our fits and do not venture to describe the spectrum of GRS1915 at energies higher than the PCA bandwidth.

Next, we explored a more physically meaningful Comptonization model, COMPTT, to fit the corona component (Titarchuk 1994; Hua & Titarchuk 1995; Titarchuk & Lyubarskij 1995). In their paper, modeling 107 spectra of GRS1915 in different spectral states, Titarchuk & Seifina (2009) showed that the photons from the disk that are scattered by the corona have a constant characteristic temperature of $T_0 \sim 1$ keV. We found that by slightly adjusting their approach so that the seed photon temperature was tied to the characteristic disk temperature $T_{\rm disk}$ (given by the component EZDISKBB), we were able to produce a satisfactory number of good fits. However, beyond this artificial scaling between the characteristic disk temperature and the seed photons, the model showed erratic behavior in T_e. In addition, both T_e and the optical depth dropped below the limit where the analytical equations break down due to upscattering inefficiency (see Figure 7 in Hua & Titarchuk 1995). For these reasons, we eschewed this model in favor of an empirical approach.

3.2. The Empirical Approach to a Power-law Component: SIMPLCUT

In order to empirically describe the curvature in the corona component within a self-consistent and flexible framework, we modified the SIMPL model (Steiner et al. 2009b) to incorporate a high-energy cutoff. SIMPLCUT is an extension of the approximate Comptonization component SIMPL with an additional parameter: a high-energy exponential folding term, $E_{\rm fold}$. The parameter Γ represents the asymptotic power law before curvature comes into effect. This model is described by Equations (3) and (4) in Steiner et al. (2009b) in tandem with an exponential folding in energy and will be described in detail in a future publication (J.F. Steiner et al. 2016, in preparation). It was incorporated in xspec as a local model. This model has the virtue of being able to operate on an arbitrary seed spectrum, and conserves photon number—as is appropriate for Comptonization. In practice, we tied the seed photons to the spectrum of the accretion disk. A fraction of the seed photons $f_{\rm sc}$ are scattered into a curved power-law shape which is locally computed for each energy. It is important to note that this enables the calculation of an *intrinsic* disk luminosity, i.e., the luminosity emitted by the disk directly, prior to any transfer or scattering that transpires in the corona. As was already mentioned, this curvature is essential to achieve successful fits with GRS1915. SIMPLCUT, like SIMPL, also eliminates the unphysical rise at the lowest energies which is endemic in the standard POWERLAW model. Our approach, though empirical and approximate, allows us to obtain self-consistent values for the disk-normalization parameter, and thereby to make physical inferences about changes and patterns in $R_{\rm in}$.

3.3. Steady-hard Model

As described in Section 2.1, the steady observations of GRS1915 naturally separate into two zones when represented in a CD or an HID (Figure 2). Due to the spectral differences in these two regimes, we fit them with slightly different models. The backbone of both models was SIMPLCUT $\otimes$ EZDISKBB.

In fitting the steady-hard data, the inclination of the system was fixed to $i = 60^\circ$ (Reid et al. 2014) while the column density was fixed at $N_H = 5 \times 10^{22}$ cm^{-2} (Lee et al. 2002 and references therein). We also tested N_H values of 4.5–7.0 $\times 10^{22}$ cm^{-2}. No noticeable changes in the parameter distributions were evident and our conclusions are not sensitive to this setting.

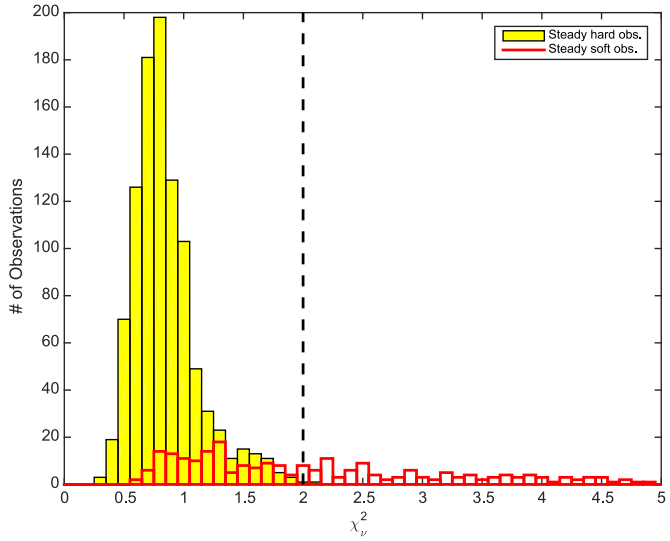

Figure 3. Distributions of χ^2_ν of steady-soft and steady-hard fits. The vertical dashed line at $\chi^2_\nu = 2$ represents the cut defined for a good-fit.

The steady-hard data were modeled via

$$\text{TBABS} \times (\text{SIMPLCUT} \otimes \text{EZDISKBB} + \text{LAOR} + \text{GAUSSIAN}).$$

The model is comprised of a number of elemental components (TBABS, Wilms et al. 2000; EZDISKBB, Zimmerman et al. 2005; LAOR, Laor 1991). Both the LAOR and GAUSSIAN line centers were fixed at 6.5 keV. The Gaussian width is forced to be very narrow (width fixed to 10 eV), corresponding to a distant, non-relativistic Fe reflection line that is sometimes observed. The addition of this component results in a 10% increase in the number of good fits. The LAOR component describes reflection in the strong-gravity regime in which extreme relativistic effects cause a red and broad distortion of the line (examples of similar broad and narrow Fe-line emission have been commonly observed in AGNs; Brenneman et al. 2014). EZDISKBB is a standard multicolor disk model for which the inner disk edge has a zero-torque boundary. This model yielded an impressive 992/993 good fits (99.9%).

The yellow filled boxes in Figure 3 show the distribution of the goodness-of-fit for the steady-hard data. It is clear that despite the strong signal, the spectral complexity, and our minimalistic models, we are able to successfully model an impressive majority of this data.

3.4. Steady-soft Model

In fitting the steady-soft data, we employed the same inclination ($i = 60°$), column density ($N_H = 5 \times 10^{22}$ cm^{-2}), and range of column density examined ($N_H = 4.5$–7.0×10^{22} cm^{-2}) as in the steady-hard observations, with no significant change in the parameter distributions observed.

As noted in Section 3.1, we tested 70 model variants on the GRS1915 spectra. This was motivated by our need to add features, investigated one at a time, to gain acceptable fits for the steady-soft spectra. This is why the models for steady-soft and steady-hard observations differ. The extra terms have also been used for soft states, when required, by other researchers (see below).

The steady-soft data were modeled using

$$\text{TBABS} \times \text{SMEDGE} \times (\text{SIMPLCUT} \otimes \text{EZDISKBB} + \text{LAOR}) \times \text{GABS}.$$

They require the addition of a smeared absorption edge (SMEDGE; Ebisawa et al. 1994, see also Sobczak et al. 1999), another feature of reflection, which onsets between 7.5 and 9.0 keV (the SMEDGE width was fixed to 7 keV). We additionally include a Gaussian Fe-absorption component (GABS) with width fixed to 0.5 keV and central energy fitted between 6.3 and 7.5 keV. Fe-absorption in this region for the soft spectra of GRS1915 has been observed in previous studies (McClintock et al. 2006) and is probably due to the presence of a strong disk wind (Kotani et al. 2000; Neilsen & Lee 2009). χ^2_ν was significantly improved by the addition of these components, although the key model parameters (i.e., the disk's normalization and temperature) were not affected.

Strong degeneracy within the model fits in the steady-soft data was revealed when attempting to determine parameter uncertainties via xspec's "error" command. In particular, we found degenerate trends allowing very high Γ and high f_{sc}, as warned against as a modeling artifact in Steiner et al. (2009b). In order to proceed, and to mitigate this complication, we found it necessary to adopt a fixed value for Γ. We investigated three values that were chosen based on the typical Γ values observed in canonical BHBs in soft states; 2.0, 2.5, and 3.0. While the parameter distributions remain relatively unaffected by the choice of value, we found that $\Gamma = 2.0$ yields a lower number of good fits while $\Gamma = 3.0$ allows observations which display degenerate tendencies. Hence, we favor $\Gamma = 2.5$.

We also observed that a lower limit to $E_{\rm fold}$ of ~10 keV is necessary for the success of this model. Although a significant number of our fits show an $E_{\rm fold}$ cluster close to our lower limit, it serves to keep the coronal component from encroaching on the accretion disk and to avoid degeneracy within our model fits.

Using this model and set of constraints, we obtained 135/264 good fits (51%) for the steady-soft observations. The red-outlined boxes in Figure 3 show the distribution of the goodness-of-fit for the steady-soft data. Admittedly, there is a broad distribution in χ^2_ν. We also acknowledge that the constraints we apply may limit the information we can obtain from our steady-soft model. However, due to the complexity of the steady-soft spectrum and the simplicity of the available models, we consider it *worthwhile* to examine the implied physical evolution of the steady-soft observations using our model.

Illustrative fits for both steady-hard (top panel) and steady-soft (bottom panel) observations are shown in Figure 4. Curvature is observed in the Compton components (see also McClintock & Remillard 2006, pp. 157–213; Neilsen et al. 2011).

4. RESULTS

In this section, we present the results of our spectral analyses. All of the results described use only the good-fit observations characterized in Section 3. We report on the steady-soft and steady-hard behavior of the accretion disk, followed by the corona, and then the radio jet. This is followed by a comparison of the observations of GRS1915 to canonical BHB states as well as to the variable states defined by Belloni et al. (2000).

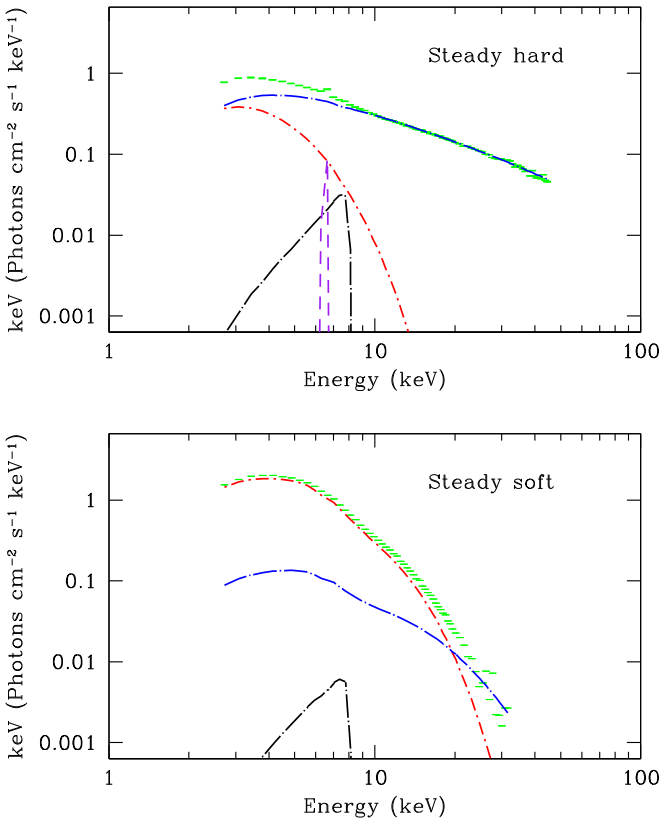

Figure 4. Two unfolded spectra which are typical and exemplify the steady-hard and steady-soft data, respectively. Top: the steady-hard spectrum for data segment 1103_a (ObsID 20402-01-10-00) for which we obtain a fit with $\chi^2_\nu = 0.76$. Bottom: the steady-soft spectrum for data segment 0881_a (ObsID 10408-01-11-00) for which we obtain a fit with $\chi^2_\nu = 0.73$. Data is represented in green, the disk component in red, and the coronal component in blue. Note the curvature in both coronal components.

4.1. The Accretion Disk

The accretion disk parameters are of central interest to our investigation. Although the two models fitted to the steady-soft and steady-hard observations are different, each incorporates the multicolor disk model, EZDISKBB (Zimmerman et al. 2005), which has two free parameters: the maximum disk temperature ($T_{\rm max}$) and a normalization parameter (K). From the normalization, it is straightforward to determine $R_{\rm in}$. We emphasize that by using SIMPLCUT, our model is self-consistent in counting Comptonized photons, which enables us to directly obtain the *intrinsic* $R_{\rm in}$ (in km) via

$$R_{\rm in} = \left(\frac{K' f_{\rm col}^4 D_{10}^2}{\cos(i)}\right)^{1/2}, \quad (1)$$

where $f_{\rm col}$ is the color correction, i is the inclination, and D is the distance to the source in kiloparsecs, where $D_{10} = \frac{D}{10}$ (distance in 10 s of kpc) and

$$K' = \frac{K}{(1 - f_{\rm sc})}, \quad (2)$$

where $f_{\rm sc}$ is the scattering fraction determined by SIMPLCUT (which is implemented so as to directly report K'). We note that many publications that do not use SIMPL or its derivative models, and thus have no means of conserving photon number, use the apparent inner disk radius ($R_{\rm app}$) for their analysis. $R_{\rm in}$ and $R_{\rm app}$ are related as

$$R_{\rm in} = \frac{R_{\rm app}}{(1 - f_{\rm sc})^{1/2}}. \quad (3)$$

$R_{\rm in}$ is calculated using a distance of $D = 8.6^{+2.0}_{-1.6}$ kpc, an inclination of $i = 60 \pm 5°$ (Reid et al. 2014), and a constant color correction factor of $f_{\rm col} = 1.7$ (Shimura & Takahara 1995). We caution that the measurements of $R_{\rm in}$ are approximate and that their accuracy is limited by the use of non-relativistic, classical models, and other simplifications including a single, static value for $f_{\rm col}$—despite the fact that it should vary with luminosity and depends upon the mass and spin (e.g., Davis et al. 2006). However, despite these uncertainties which may affect the scaling, our primary interest in the radius measurements is to test for large-scale variations, for which these higher-order modifications are moot.

Figures 5 and 6 show the relationship between the disk temperature, the inner disk radius, the disk luminosity, and the mass accretion rate. The mass accretion rate through the accretion disk is determined by

$$\dot{M} = \frac{2 L_{\rm disk} R_{\rm in}}{GM}, \quad (4)$$

where

$$L_{\rm disk} = 73.9 \sigma \left(\frac{T_{\rm max}}{f_{\rm col}}\right)^4 R_{\rm in}^2 \quad (5)$$

(see Mitsuda et al. 1984; Makishima et al. 1986). Red points (upper panels) represent the steady-soft observations while black points (lower panels) represent the steady-hard observations. The relationships between these accretion disk parameters obtained using both steady-soft and steady-hard observations show reasonably ordered branches. We remind the reader that these branches observed are not necessarily time-ordered. They simply represent a collection of steady-state data. In real time, the source can disappear from these diagrams into variable states and later reappear at a different steady location.

4.1.1. The Steady-soft Accretion Disk

Figure 5 displays a four-cell grid of plots where we present the changes in $R_{\rm in}$ as a function of two quantities: luminosity (expressed as a fraction of the Eddington limit) and mass accretion rate through the disk. The upper panels and lower panels show the steady-soft (red circles) and steady-hard (black squares) observations, respectively. Mean error bars for each plot are indicated in the right-hand bottom corner. Here and throughout this article, all of the errors presented describe 1σ confidence intervals.

A large majority of the steady-soft observations (96%) display a roughly constant $R_{\rm in}$, which is strongly reminiscent of the canonical BHB soft state (see also Tanaka & Lewin 1995, p. 126). Given the constancy of this branch over the large range of luminosities, its $R_{\rm in}$ likely corresponds to $R_{\rm ISCO}$ for GRS1915. The slightly upward trend for $R_{\rm in}$ at higher luminosities (upper panels in Figure 5) is reminiscent of the "spin droop" that has been observed in several BHBs including GRS1915 itself (McClintock et al. 2006; see also Steiner

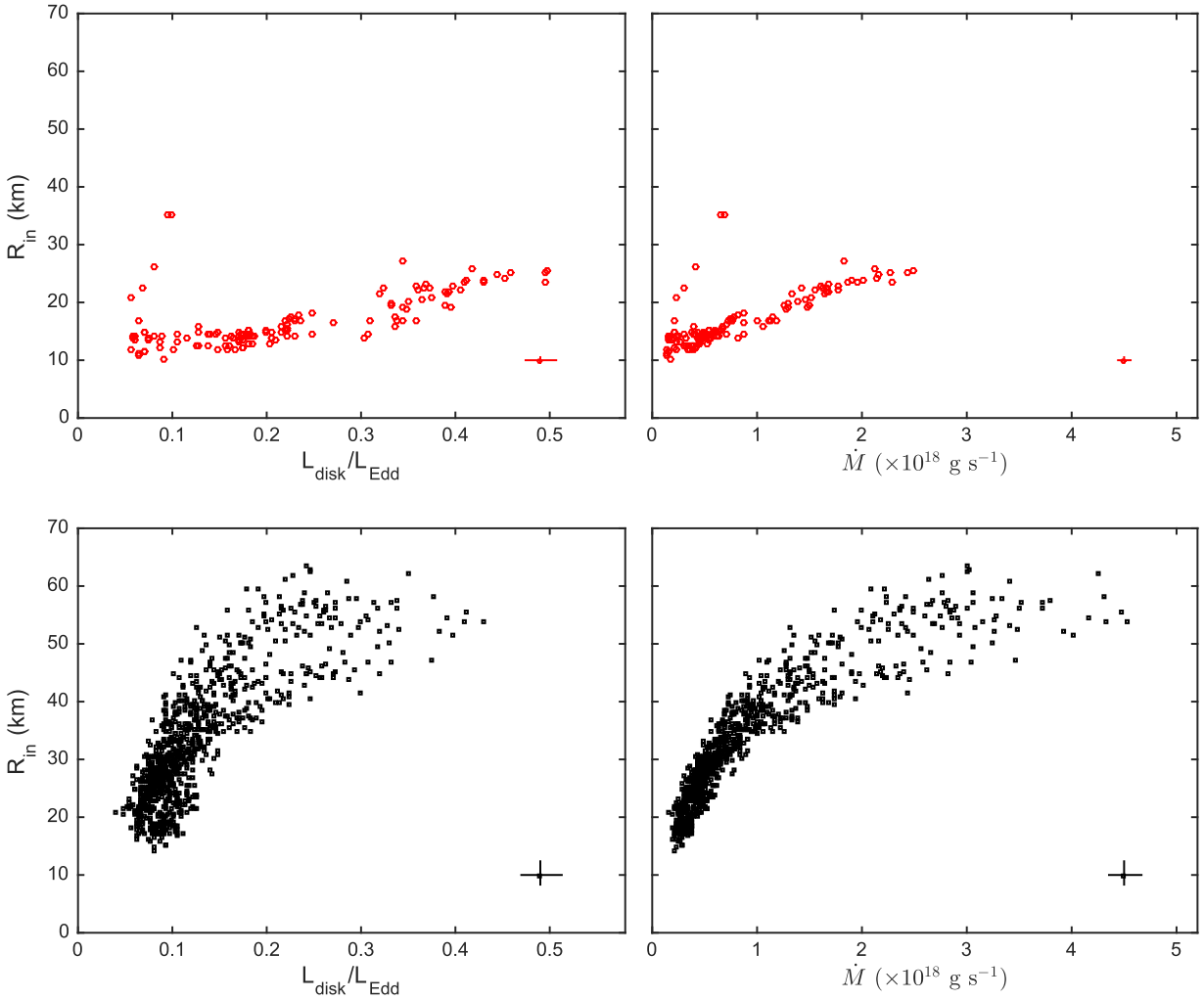

Figure 5. $R_{\rm in}$ as a function of the disk luminosity ($L_{\rm disk}/L_{\rm Edd}$, where $L_{\rm Edd} \approx 1.3 \times 10^{38}(M/M_{\odot})$ erg s^{-1}; Frank et al. 1992) and mass accretion rate ($\dot{M}$). Top panels: the steady-soft observations represented by red circles. A branch showing approximately constant $R_{\rm in}$ is apparent. A few observations which show departure to larger $R_{\rm in}$ are present at low luminosity. Bottom panels: the steady-hard observations represented by back squares. An organized increase in $R_{\rm in}$ with increasing $L_{\rm disk}/L_{\rm Edd}$ and $\dot{M}$ is observed. The mean 1σ error bars are indicated in the right-hand bottom corner of each plot. The full uncertainties (i.e., inclusive of the error due to distance and inclination) in the steady-soft and steady-hard parameters are as follows: $R_{\rm in} \sim 26\%$, $L_{\rm disk} \sim 55\%$, and $\dot{M} \sim 90\%$.

et al. 2010, 2011). For this source, it is not likely to be caused by change in $f_{\rm col}$ (see also Done et al. 2007). It could instead be the result of a "local Eddington effect" (Lin et al. 2009) tied to the maximum and roughly constant inner disk temperature seen at $L_{\rm disk} > 0.2L_{\rm Edd}$ (see below). We cannot separate this effect from any structural changes in the disk that may occur at high $L_{\rm disk}$.

At least six observations at low luminosity show a departure to larger $R_{\rm in}$ compared to the constant $R_{\rm in}$ branch.[7] Amidst our quest for quelling degeneracy in our choice of steady-soft model (see Section 3.4), we investigated the possibility that these points may be erroneous. However, our analyses revealed these points to be just as robust as all of the other points which exhibit a more canonical result. Therefore we proceed, albeit with caution, to treat them as good fits and include them in our analysis in Section 5. We also note that these points seem to lie in the $L_{\rm disk}$–$R_{\rm in}$ space that is occupied by the steady-hard observations. However, their classification is unambiguously steady-soft, as is further shown in Section 5.

[7] These are not the points at [0.4, 1.55] in the CD that were close to the line between the hard/soft classification.

Following the format of Figure 5, in Figure 6, we present a second four-cell grid of plots that displays the changes in $T_{\rm max}$ against the same two quantities as before, luminosity and mass accretion rate through the disk. The steady-soft observations (upper panels of Figure 6) show temperatures between 1 and 2.4 keV (consistent with those observed by Muno et al. 1999 for observations with no quasi-periodic oscillation, QPOs, see their Figure 8(b)) with the constant $R_{\rm in}$ branch featuring higher temperatures of ∼2 keV. These temperatures are significantly higher than observed in other canonical BHB disks, for which a peak temperature of $\leqslant$1 keV is typical (e.g., RM06). The observations at low luminosity which show departure to larger $R_{\rm in}$, also display the lowest temperatures.

4.1.2. The Steady-hard Accretion Disk

The lower panels of Figure 6 show the temperature of the inner disk for the steady-hard observations. They show a mean disk temperature of 1.19 ± 0.12 keV, corroborating the results of earlier studies which suggest the presence of a hot disk even in the harder observations of GRS1915 (Muno et al. 1999). This enables us to detect and measure the properties of the

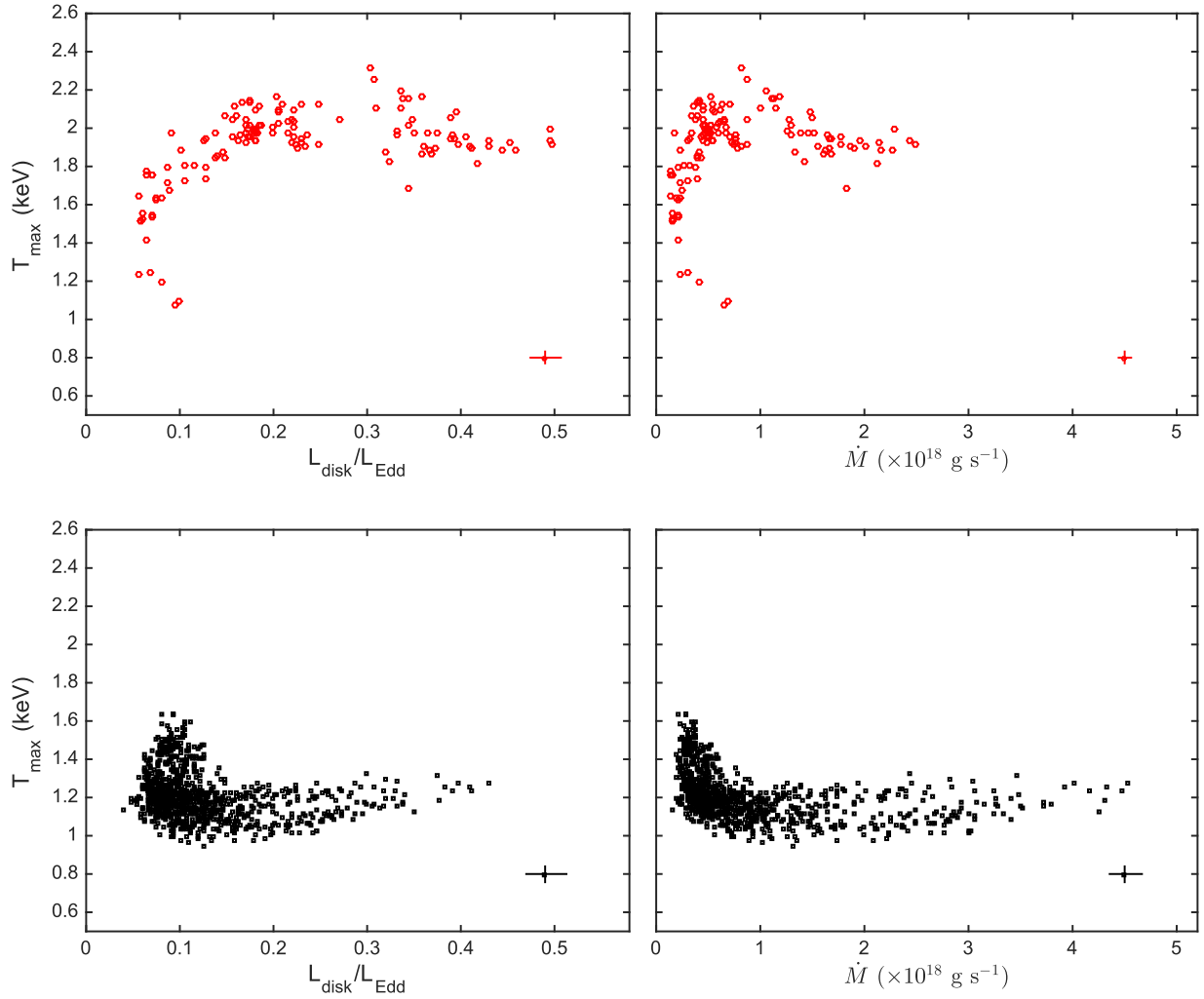

Figure 6. $T_{\rm max}$ as a function of $L_{\rm disk}/L_{\rm Edd}$ and $\dot{M}$. The top and bottom panels show, respectively, steady-soft and steady-hard observations, as in Figure 5. Mean 1σ error bars are indicated as in Figure 5.

inner disk and to explore its behavior. The most striking result (see Figure 5) is that $R_{\rm in}$ for the *steady-hard* data increases with growing disk luminosity and mass accretion rate, demonstrating an evolving, truncated disk.

Increases in $R_{\rm in}$ at much shorter timescales have been observed in the variable states of GRS1915 (β state, Belloni et al. 1997a, 1997b; ρ state, Neilsen et al. 2011), suggesting a possible phenomenological link between the long (>2.1 ks) and short (∼10 s of seconds) timescales in the system. This link will be further evaluated in Section 5.

Several processes can be hypothesized as possible causes for this truncation and scaling:

1. a local Eddington effect for a thin disk;
2. an advection-dominated accretion flow (ADAF);
3. a magnetically arrested disk (MAD).

A local Eddington effect has been invoked to interpret those observations in which the inner disk reaches a maximum temperature, and further increases in luminosity are accounted for by increases in the disk radius at constant (maximum) temperature. Examples are several types of behavior in the accreting neutron star subclass known as Z-sources (Lin et al. 2009) and the behavior of the disk in GRS1915 during the ρ state variability cycles (Neilsen et al. 2011). This concept was mentioned in the context of the gradient of the roughly constant $R_{\rm in}$ branch of the steady-soft observations in Section 4.1.1. However, Figures 5 and 6 show that the steady-hard observations showing radius expansion exhibit temperatures a factor of two lower than the maximum temperatures observed in the system, and so we conclude that a local Eddington effect is not a viable explanation for radius expansion in steady-hard conditions.

An ADAF is characterized by a low-density, optically thin, quasi-spherical flow where most of the viscous energy released does not radiate efficiently, resulting in the energy being advected into the black hole. The ADAF model offers an alternative solution to accretion in a thin disk, but the transition radius that may separate these accretion geometries must be determined empirically, rather than by deterministic factors (e.g., Esin et al. 1997). Given the organized behavior of the steady-hard truncated disk (Figure 5), it would appear that the ADAF hypothesis, in and of itself, is incomplete. In the absence of an ADAF transition mechanism that moves outward with growing disk luminosity, we do not discuss this alternative further.

The idea that global magnetic field properties may play a role in distinguishing steady-soft and steady-hard conditions and magnetically truncate the accretion disk (Narayan et al. 2003;

Tagger et al. 2004) is plausible. The concept here is that a vertical or poloidal magnetic field may be entrained into the inner disk region and then modify the geometry and energetics of the final stages of accretion. This is given further consideration in our Discussion (Section 6.3).

In Figure 5 (lower panels), we note a possible bifurcation in the steady-hard data points when GRS1915 becomes luminous, $L \geqslant 20\%$ Eddington. The hint of split $R_{\rm in}$ tracks maps to a similar appearance of splitting in the disk temperatures shown in Figure 6. We know of no clear explanation for such a phenomenon, if it is real.

4.2. The Disk–Corona Relationship

While the origin of the soft X-ray component observed in BHB spectra has been generally agreed upon as thermal radiation from an accretion disk, the origin of the hard X-ray component (power law or cutoff power law) is still poorly understood. The prevalent paradigm has been inverse-Compton scattering in a nebulous plasma referred to as the corona. In this scenario, the seed photons are from the inner disk, but the origin and geometry of the corona is uncertain (e.g., Poutanen 1999).

In Figures 7(a) and (b), we explore the connection between the accretion disk and the corona. The use of the model SIMPLCUT enables us to obtain the fraction of photons from the disk that contribute to the coronal flux ($f_{\rm sc}$). This fraction is represented as a function of the coronal flux integrated over the range 0.1–100 keV. In Figure 7(a), $f_{\rm sc}$ stays low within the steady-soft observations. In the steady-hard observations, $f_{\rm sc}$ is unusually well-behaved, holding steady between 0.2 and 0.5.

Figure 7(b) shows the division of spectral energy between the disk and coronal components. The steady-soft observations show comparatively low coronal flux and weak correlation between the disk and coronal components, with a slight growth in the contribution from the corona at high disk luminosity. While we fix Γ at 2.5 for the fits represented here (see Section 3.4), we note that the coronal flux slightly decreases if a lower power-law index ($\Gamma = 2$) is used. However, as stated in Section 3.4, the coronal flux distribution remains unchanged. In contrast, the steady-hard observations exhibit a more luminous corona and a strong correlation between the component fluxes (Figure 7(b); black points). The differences between these two tracks, despite considerable overlap in the flux from the accretion disk, could be taken to suggest that the coronae in the steady-soft and steady-hard conditions have different origins.

The strong correlation of the disk and coronal fluxes in the steady-hard observations suggests a connection between the processes that govern their production in GRS1915. Due to the extreme faintness of their disks, canonical BHBs in the hard state usually exhibit a nearly vertical track in the coronal flux versus disk-flux diagrams (see RM06). However, this correlation of disk and coronal flux might be a common feature of BHBs, which is undetected in canonical sources due to the faintness of their disks. X-ray observations of hard-state BHBs with instruments sensitive to lower energies (e.g., NICER) will shed light on this matter in the future.

4.3. The Steady-hard Corona

Due to the constraints enforced on the steady-soft model (discussed in Section 3.4), we focus on the steady-hard observations in order to explore the coronal parameters. The distributions of these parameters appear more complex and varied than those of the accretion disk parameters.

In Figures 7(c) and (d), we explore how the parameters related to the steady-hard coronal component, namely, $E_{\rm fold}$ and Γ, vary as a function of coronal flux. Most of the steady-hard observations (80%) show a power-law index in the range $1.4 < \Gamma < 2.1$, which is one of the signatures of the canonical hard state (RM06). A more complete assessment of this is given in Section 5.

We note the presence of a sub-population of points at low coronal flux that have significantly high $E_{\rm fold}$ values compared to the norm while also displaying well-constrained Γ values ($\sim$1.7) with much less scatter. These observations display a shift toward more typical hard-state coronal characteristics (see Section 6.4). Although they occur at low flux values, the high $E_{\rm fold}$ observations typically have $\sim$2.7 million counts per spectrum and their fits have been verified using the error command on xspec. The remaining observations display low $E_{\rm fold}$ values (between 10 and 30 keV), confirming the significant curvature in the Compton component within the PCA bandpass (Figure 7(c)). $E_{\rm fold}$ shows no obvious correlation with coronal flux. Γ shows an overall increase with growing coronal flux (Figure 7(d)).

We observe indications of the existence of two (or maybe more) coronal tracks within the steady-hard observations in both $E_{\rm fold}$ and Γ plots. We note the presence of two tracks at higher luminosities in Figure 7(c) and two tracks with differing slopes in Figure 7(d). These tracks approximately match the set of tracks in Section 4.1.2, but do not map one-to-one. Further interpretation of this splitting is left for future work.

4.4. The Radio Jet

In this section, we consider all of the radio observations that time-match (within $\pm$0.5 days) the steady-soft (70) and steady-hard (624) X-ray observations (see Section 2.2).

We first examine how the radio flux levels differ in the steady-hard and the steady-soft observations. In Figure 8, we show the radio flux (represented in log scale) as a function of time. We find that 95% of the steady-hard data points have radio flux $>$5 mJy, with the maximum radio flux exceeding 100 mJy at times. 99% of the steady-hard data points have radio flux $>$2 mJy (consistent with Muno et al. 2001; Klein-Wolt et al. 2002). In the steady-soft data, we conversely find that 77% have radio flux $<$2 mJy and 99% have radio $<$5 mJy. Our observations substantiate the idea that the steady-hard observations are associated with a radio jet. Some steady-soft observations show the presence of radio flux at lower levels. However, this low radio flux does not show any clear relation to the steady-soft disk or corona. Furthermore, at low radio flux, there is a chance that some portion of the emission arises from jet material that is detached from the core. This issue cannot be further investigated with these data given their insufficient spatial resolution. Hence, we focus on the radio jet behavior of only the steady-hard observations.

4.5. The Corona–Jet Relationship

Strong coupling of the hard X-ray flux and the jet, inferred from theory and observed in data (e.g., Fender et al. 1999a; Poutanen 1999), supports the proposition that in hard states, the corona is associated with the base of the jet. The importance of this coupling is evident in the work by Gallo et al. (2012) in

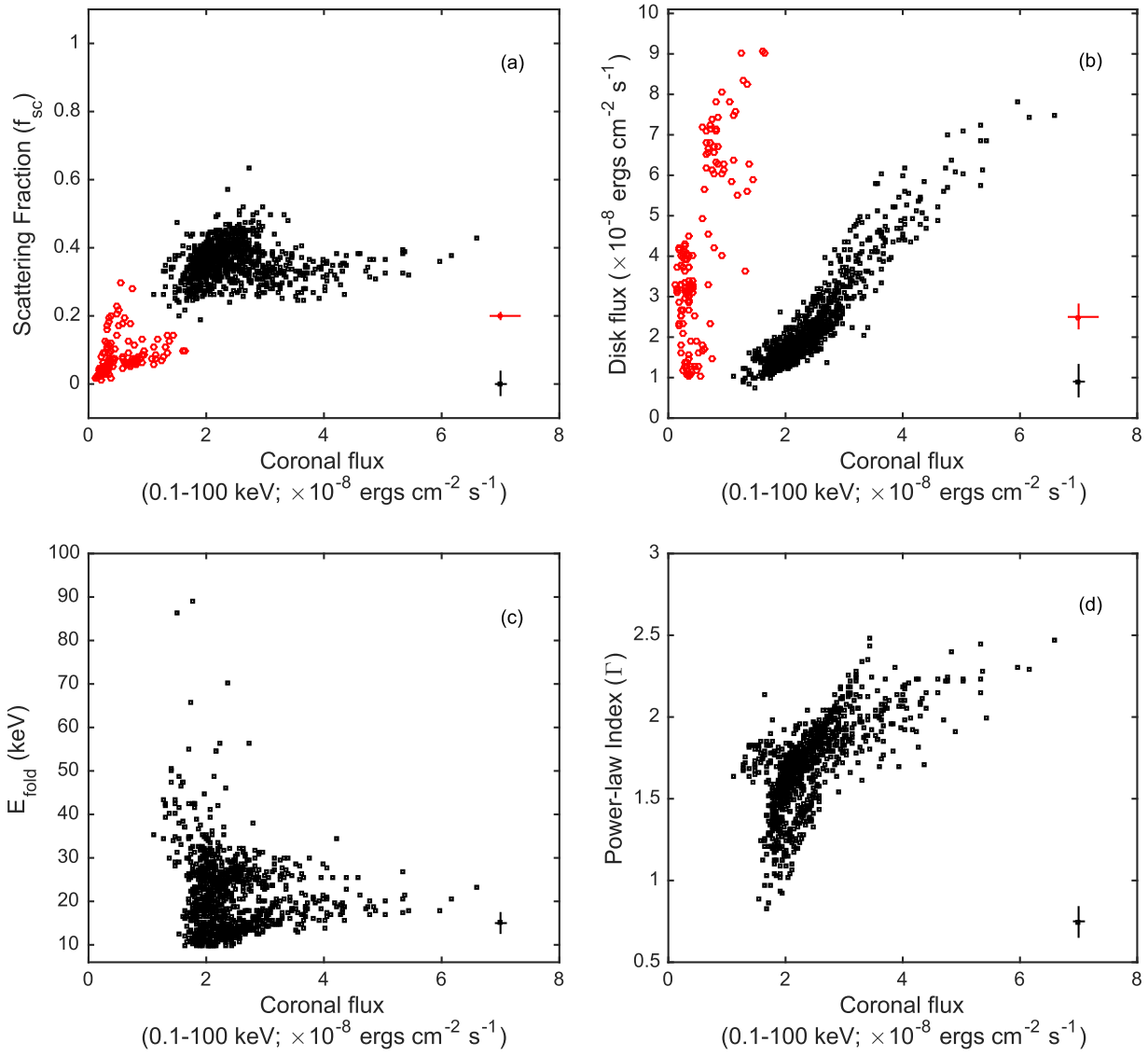

Figure 7. Top panels: (a) Scattering fraction (f_{sc}) and (b) disk flux as a function of coronal flux in both steady-soft (red circles) and steady-hard (black squares) observations. Bottom panels: (c) E_{fold} and (d) Γ as functions of coronal flux in the steady-hard observations.

uncovering two tracks relating the X-ray and radio luminosities in multiple BHB systems. The study of this hard X-ray/radio connection may shed light on the process of jet formation.

We isolate the coronal luminosity in the steady-hard observations of GRS1915, which produced good fits (992/993), and investigate its behavior in response to the radio jet. Figure 9 shows the radio luminosity as a function of the 1–10 keV X-ray luminosity.[8] We also overplot the Gallo et al. (2012) tracks (hereafter G12 tracks) in red (0.63 slope track) and blue (0.98 slope track). Taken as a whole, no obvious correlations are apparent. However, we identify three regions of interest: (1) the region with lowest coronal luminosity, which seems to display a trend that matches the G12 tracks; (2) the region with highest radio luminosity, which corresponds to a subset of the radio plateau state observations; and (3) a diffuse region with high coronal luminosity, which will be addressed in Section 4.6 (encircled by a green dashed line in Figures 9 and 12). In the following paragraphs, we will discuss (1) and (2) in the context of recent literature.

The top two panels of Figure 10 show the steady-hard X-ray light curve in energy bands of 2.2–8.6 keV and 8.6–18.0 keV. We note the presence of two time periods when the count rate gradually decreases to low values in both bands. The first of these dips was categorized by Belloni et al. (2000) as the χ_2 class. The bottom panel in Figure 10 shows the radio light curve, which indicates that the radio luminosity corresponding to the decline into these X-ray dips is also relatively invariant. As the X-ray count rate rises out of these light-curve dips, the radio luminosity shows large variability (~1 order of magnitude). We neglect any such highly variable points. The points in the X-ray dips corresponding to the luminosity decline are isolated and shown in cyan in both Figures 9 and 10. They are defined by the time ranges given in Table 1. Interestingly, we find that these points happen to lie almost exactly on the upper G12 track (red line in Figure 9). A fit to these points yields a log slope $\eta \sim 0.68 \pm 0.35$ (with the intercept at 5.32 where $L_X \propto L_R^{\eta}$). This is consistent with the

[8] To be consistent with the results of Gallo et al. (2012), we use 1–10 keV integrated luminosities for this section.

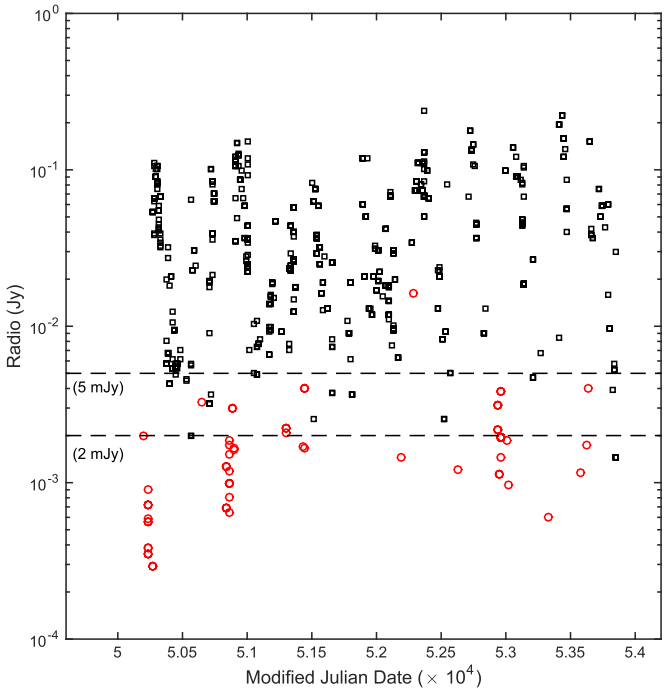

Figure 8. Ryle telescope 15 GHz radio light curve of GRS1915's jet activity. Black squares show the radio flux corresponding with steady-hard observations and the red circles correspond to steady-soft observations (i.e., within ±0.5 days of the X-ray point). The dashed lines mark our reference flux levels of 5 and 2 mJy. There is a clear difference in the brightness of the steady-hard compared to steady-soft data. We note that several steady-soft observations are not represented here due to extremely weak radio detections, or even non-detections. The single radio-bright steady-soft observation was tightly sandwiched between two hard states. Emission from jet material disconnected from the core possibly explains its higher radio flux. For reference, the typical error associated with each data point is ∼±0.5 mJy.

slope of the upper G12 track, $\eta = 0.63$. However, we note that the uncertainty associated with our measurement is quite large. These points, hereafter referred to as "G12-like" points, also exhibit high $E_{\rm fold}$ values while showing Γ values clustered tightly about ∼1.8, as is typical for a canonical hard state. The G12-like points suggest that as the system declines to lower X-ray luminosities, the steady-hard observations exhibit parameter values which are more typical of a canonical BHB hard state.

The second region of interest is the set of points which are a subset of the radio plateau states of GRS1915, which were previously selected for an independent X-ray–radio study by Rushton et al. (2010). We used *RXTE*/PCA observations with simultaneous radio data (see Section 2.2) time matched within ±0.5 days to the times of the their *RXTE*/ASM observations (Rushton et al. 2010, private communication). Hereafter, we refer to them as "R10" points. They are represented by the purple triangles in the upper half of Figure 9. A fit to the purple triangles in our plot yields a log slope of $\eta \sim 1.12 \pm 0.13$ (with the intercept at -10.28) showing a higher slope with respect to the G12-like points.

In their study, Rushton et al. (2010) obtained a log slope of $\eta \sim 1.7$. Their use of *RXTE*/ASM data necessarily limited their computation to an energy band of 2–12 keV and their analysis included both disk and coronal components. Our value is derived using the isolated coronal component luminosity (i.e., removing the contaminated disk contribution), integrated from 1 to 10 keV. It is therefore more suitable for comparison with the power-law-dominated BHB hard-state luminosities used by Gallo et al. (2012).

In Figure 11, we show the relationship between the radio luminosity and the model parameter $E_{\rm fold}$. $E_{\rm fold}$ is the only parameter that displays a simple relationship to the radio luminosity, showing a strong nonlinear anti-correlation. This anti-correlation nicely separates the G12-like points (cyan squares) and the R10 points (purple triangles), with the former having the highest $E_{\rm fold}$ values and the latter having the lowest $E_{\rm fold}$ values. The high $E_{\rm fold}$ values of the G12-like points indicate a hotter corona that is more consistent with a canonical hard state. The low $E_{\rm fold}$ values displayed by the R10 points and the anti-correlation itself are still puzzles.

4.6. A Possible Connection between the Accretion Disk and the Radio Jet

In Figure 12, we represent the two regions of different jet activity discussed above in the context of the relationship between the coronal flux and the inner disk radius. It is interesting to note that both regions of jet activity that display correlations to coronal luminosity occur when the steady-hard disk has low $R_{\rm in}$. They also appear to be linked to two tracks in Figure 12. It is also noteworthy that the black data points in Figure 9, situated between the G12-like region and the R10 region and outside the dashed green circle, display mid-range $E_{\rm fold}$ values and form a track in Figure 12 which exists in the middle of the purple and cyan tracks.

The apparent link of the two jet activity regions (cyan and purple points) to the two tracks does not hold at high $R_{\rm in}$. The extension of cyan and purple points in Figure 12 is very different from the extension of the same in Figure 9. While the cyan and purple points appear to be fairly organized in both Figures, any possible tracks within the green area in Figure 12 (high $R_{\rm in}$) are completely mixed when traced back to Figure 9. In summary, we note that while there appears to be a connection between the radio jet and the inner radius of the disk, the radio jet seems to be a function of other parameters which are presently unknown.

5. RIGOROUS COMPARISON TO CANONICAL BHB STATES

In their review of BHBs, RM06 define three BHB spectral-timing states: thermal, SPL, and hard. The criteria for each are given in their Table 2 and are based on the characteristics of the X-ray spectra, PDS, and QPOs. In this section, we explore our observations of GRS1915 within their widely used state framework.

We took each X-ray observation and its corresponding PDS and matched their parameters to the criteria defining each state. Observations that matched the thermal criteria were represented as red crosses while observations that matched the SPL and hard criteria were represented as green triangles and dark blue squares, respectively. The SPL state observations were split into two groups, with those displaying low-frequency QPOs (LFQPOs; <30 Hz) represented by filled green triangles (referred to as SPL-qpo) and those without LFQPOs marked with open green triangles (referred to as SPL-noqpo). Observations with parameters that did not fit within the boundaries of the state classifications were marked with black open circles. In addition, any steady-hard observations that did

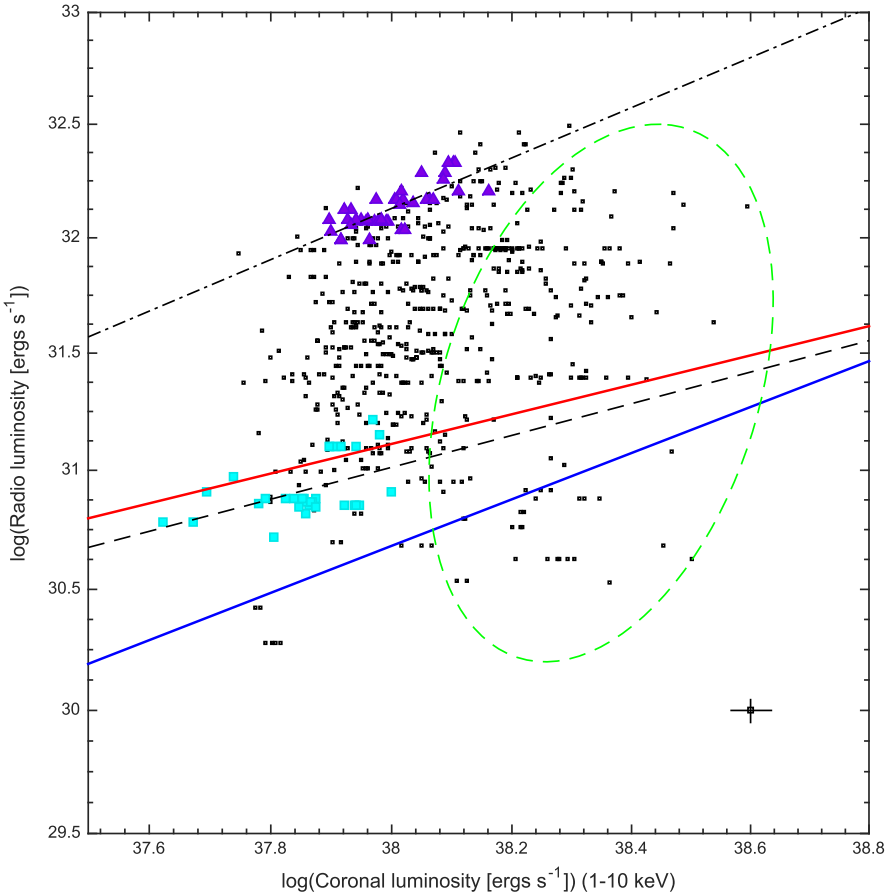

Figure 9. Radio vs. coronal luminosity. Cyan squares represent the G12-like points on the decline of the steady-hard light-curve dips observed within the time periods specified by Table 1. Purple triangles represent the R10 points. The red and blue lines represent the G12 tracks ($L_r \propto L_X^{\eta}$ where $\eta = 0.63$ and 0.98). The dashed line represents the fit to the cyan squares ($\eta \sim 0.68 \pm 0.35$) and the dot–dashed line represents the fit to the purple triangles ($\eta \sim 1.12 \pm 0.13$). The region encircled by the dashed green line will be explained in Section 4.6.

not fit the hard-state disk fraction[9] ($f_{\rm disk}$) constraint of $f_{\rm disk} < 20\%$ (see Table 2 in RM06) but fit all of the other hard-state criteria were represented as cyan squares. The resulting mapping of these data onto RM06 states is shown in Figure 13, depicting $R_{\rm in}$ versus disk luminosity.

A majority of the steady-soft data match either thermal (43%) or SPL (13%) states, while the remainder have one or more parameters with values that are outside of the criteria of the three states explored. The thermal states line up nicely, dominating the constant $R_{\rm in}$ branch. This is consistent with the observations of canonical BHB thermal states that show $R_{\rm in}$ going down to $R_{\rm ISCO}$ (e.g., Steiner et al. 2009a).

Among the steady-hard observations, we find a few (0.01%) that are consistent with the hard state. However, we find that when the disk fraction is neglected, a majority of the steady-hard observations (80%) are found to match the hard-state criteria (cyan points in Figure 13). The higher disk fraction in GRS1915 is a consequence of the unique presence of a hot and bright disk in the steady-hard observations, as determined from our spectral fits. The alignment of the other parameters (rms power, spectral index, and QPO behavior) with the well-studied states in many other black hole systems confirms the posited association between the steady observations of GRS1915 and the canonical black hole states.

When compared, the two groups of SPL observations display several distinct differences in characteristics in addition to the LFQPO presence. SPL-noqpo includes the observations that show departure in $R_{\rm in}$ (see Section 4.1.1). It also materializes at lower luminosities compared to SPL-qpo, as seen clearly in Figure 13. Furthermore, SPL-noqpo displays lower integrated rms power (0.1–10 Hz) and higher scattering fraction ($f_{\rm sc}$) when compared to SPL-qpo.

Figure 14 shows the normalized CD with data points color-coded for states, as described above (see Figure 2). The thermal and the SPL-qpo observations cluster together displaying higher HR1 compared to the SPL-noqpo observations. Remarkably, the locations of the two resultant CD clusters appear to be similar to the those of the A and B regions defined for GRS1915's *variable* observations by Belloni et al. (2000, see their Figure 8). While the cluster comprised of the thermal and SPL-qpo observations maps to B, the SPL-noqpo observations appear in a location similar to A. The steady-hard observations map to the location of the C variable state. If such a link exists between the steady observations and the transient A, B, and C states, then it demonstrates a compelling link between short and long timescales in GRS1915's phenomenology.

[9] Here, to be consistent with RM06, we use the disk fraction calculated using the apparent disk flux divided by the sum of the apparent disk and coronal flux, all in the 2–20 keV flux bands.

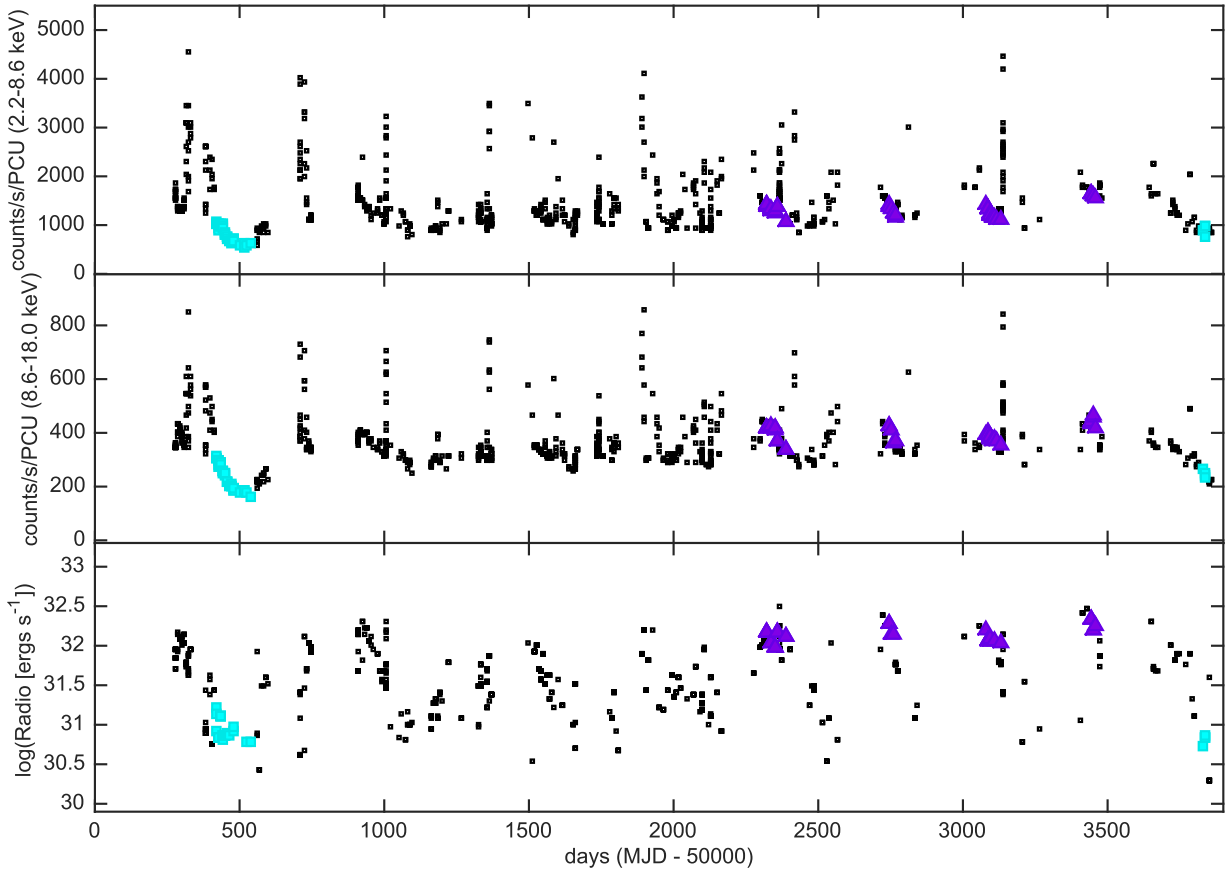

Figure 10. X-ray and log(radio) light curves with G12-like points and the R10 points colored in cyan and purple, respectively.

Table 1
Time Ranges Used to Obtain G12-like Points

Start Date	End Date	# of Obs.
50420	50550	27
53820	53850	4

6. DISCUSSION

In this section, we discuss our confidence in our models and the implications of our results. We first establish our confidence in the models used in this paper by exploring several aspects of their performance. We then move on to discuss the results which they have enabled us to obtain. First, we discuss the behavior of the accretion disk in the steady-soft observations. Next, we discuss a MAD as a possible scenario to explain the disk truncation observed in the steady-hard observations. We then discuss the X-ray–radio correlations we observe, followed by the possible effects due to high spin.

6.1. Model Confidence

Our adopted spectral models combine the paradigms of BHB accretion research with pragmatic adjustments to gain acceptable model fits. Since the models are not unique, we must evaluate the results on performance issues, e.g., their ability to provide physical parameters that are self-consistent, robust in handling the large range in source luminosity, productive in gaining insights into source behavior, and capable of showing correlations with measurements independent of the spectral fits.

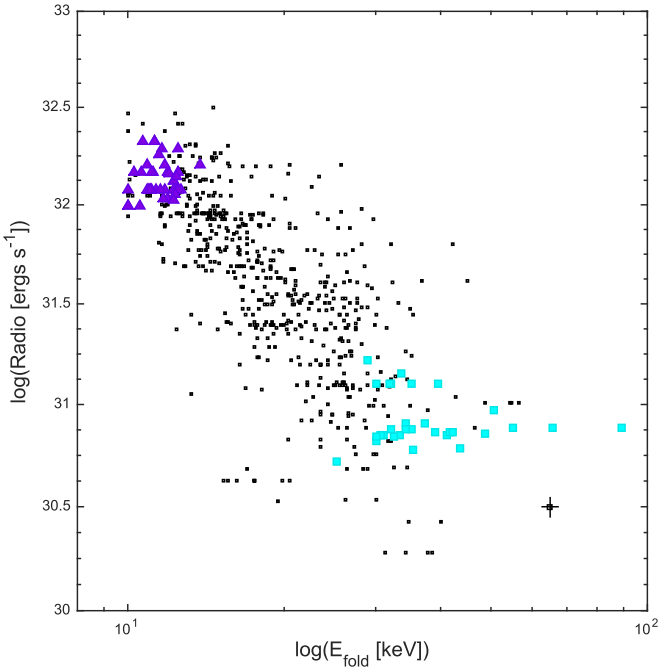

Figure 11. $E_{\rm fold}$ as a function of radio luminosity. The colors represent the populations described in the caption of Figure 10.

As shown in Section 3.2, we used two slightly different spectral models to fit the steady-soft and steady-hard observations. In the steady-hard observations, we observe that $R_{\rm in}$ drops to ∼15 km when closest to the black hole. This is

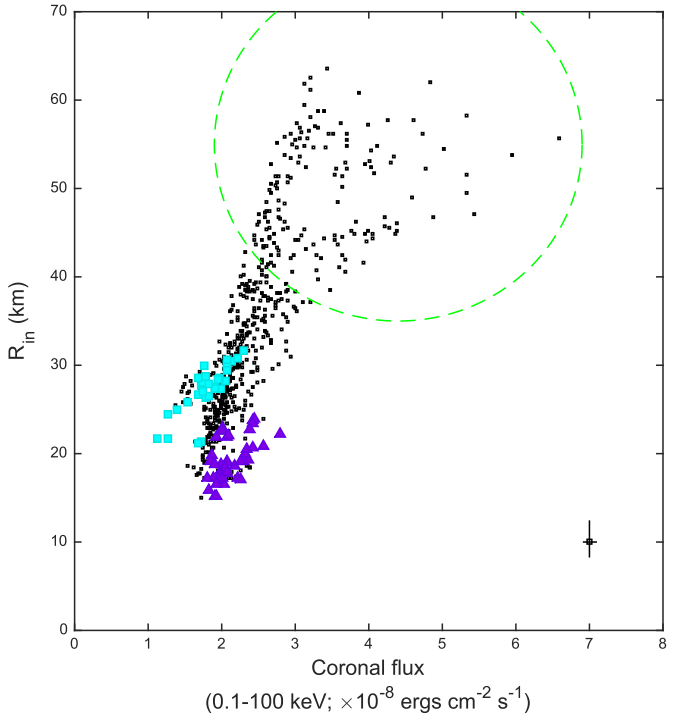

Figure 12. Variation of $R_{\rm in}$ as function of coronal flux. As in Figure 11, the colored points represent the selections in Figure 10. The dashed green line roughly outlines the same points as in Figure 9. The apparent link of the two jet activity regions (cyan and purple points) to the two tracks does not hold in this region.

consistent with the $R_{\rm in}$ observed in the steady-soft data showing a self-consistent picture of $R_{\rm in}$ across both models.

Our observation of a roughly constant $R_{\rm in}$ branch in the steady-soft observations of GRS1915, over a wide range of luminosity, strengthens our confidence in the robustness of our model to handling changes in source luminosity. The minority of steady-soft observations that deviate from the main branch and show increasing $R_{\rm in}$ have common properties; they are in the SPL state on the basis of a low disk fraction in energy flux, rather than the alternative path that is based on the presence of LFQPOs.

In order to explore parameter correlations with measurements independent of the fits, we turn to timing information within the steady-hard observations. 100% of the steady-hard PDS display a strong LFQPO (∼0.1–10 Hz). We separate them into two groups based on the shape and maximum frequency of the LFQPO. Type 1 consists of single-peak, low-amplitude, higher-frequency LFQPOs with no harmonics, and Type 2 characterizes high-amplitude, lower-frequency LFQPOs accompanied by one or two harmonics.

In Figure 15, we represent observations corresponding to Type 1 and Type 2 LFQPOs colored in orange and purple respectively, within a plot showing $R_{\rm in}$ as a function of the coronal flux. The Type 1 and Type 2 LFQPO observations separate to low and high radii, respectively. This shows that the timing information is tied to the structure of the inner disk as inferred from spectral results. The correlation of the model-dependent $R_{\rm in}$ with independent LFQPO properties bolsters our confidence in our steady-hard model.

We also explored the robustness of our main results (i.e., an approximately constant $R_{\rm in}$ branch in the steady-soft observations and a disk truncation in the steady-hard observations) by investigating the parameter distributions in other tested models that fell short of our expectations and were not used in our analysis. We derived and compared the apparent $R_{\rm in}$ and $L_{\rm disk}$ of our SIMPLCUT ⊗ EZDISKBB models with models that used components such as POWERLAW ⊗ HIGHECUT and COMPTT. The $R_{\rm in}$ distributions produced by these models were found to reflect our main results for both steady-soft and steady-hard data sets. Such robust results, even though these models did not return sufficient good fits, strengthens our confidence in our SIMPLCUT ⊗ EZDISKBB models.

6.2. Behavior of the Accretion Disk in the Steady-soft Observations

Tanaka & Lewin (1995, p. 126) observed for three systems that $R_{\rm in}$ is remarkably constant over a wide range of bolometric disk flux. They associated this constant $R_{\rm in}$ with the radius of the innermost stable circular orbit ($R_{\rm ISCO}$). An alternative manner of displaying the same result is to plot the disk luminosity versus temperature, which approximately goes as $L_{\rm disk} \propto T^4$ for constant $R_{\rm in}$ (Gierliński & Done 2004; Kubota & Done 2004; Done et al. 2007). Since then, the stability of $R_{\rm in}$ when the system displays a soft state has been observed for many BHB systems and is regarded as a common trait of the soft thermally dominated state of BHBs. The validity of the claim of this stable $R_{\rm in}$ as $R_{\rm ISCO}$ is bolstered by the many recent and successful spin measurements that are based on this assumption (McClintock et al. 2006; Shafee et al. 2006; Kolehmainen & Done 2010; Steiner et al. 2011, 2012, 2014).

In Figure 5, we observe a similar trait displayed by 96% of the observations. It serves as a reminder that along with its intense variability, GRS1915 also displays properties similar to canonical BHBs.

Within this roughly constant $R_{\rm in}$ branch, we note a slight increase in $R_{\rm in}$ when the luminosity rises above 0.3 $L_{\rm disk}/L_{\rm Edd}$. This increase is manifested in the "spin droop" found in several black hole systems including GRS1915 itself (e.g., McClintock et al. 2006; Steiner et al. 2010, 2011; McClintock et al. 2014), and may mark the onset of slim-disk effects (Sądowski 2009; Sądowski et al. 2011; though see Straub et al. 2011). The increase in $R_{\rm in}$ at high luminosities results in a decrease in the inferred spin value, which was apparent in the inconsistency of the two spin measurements for GRS1915 by McClintock et al. (2006) and Middleton et al. (2006; see McClintock et al. 2006 for details). Considering that the approximately constant $R_{\rm in}$ branch also displays nearly constant temperature, which also is the highest temperature observed within the steady observations (Figure 6), the increase in $R_{\rm in}$ (and corresponding "droop" in spin) might also alternatively be a result of a "local Eddington" effect much like that of the flaring branch of Z-sources (Lin et al. 2009).

6.3. A Possible Magnetic-field Controlled Truncation in the Steady-hard Observations

In this section, we further discuss the idea presented in Section 4.1.2, namely, that global magnetic field properties may be the mechanism distinguishing the steady-soft data from the steady-hard data and that the magnetic state of the disk may account for its truncation when steady-hard.

Both theory and 3D magnetohydrodynamical simulations have predicted that the accumulation of a strong poloidal magnetic field close to the black hole can disrupt the accretion

Table 2
Observation List

Reference[a]	MJD[b]	MET[c] Start	MET[c] Stop	Exposure (s)	Type	Spectral fit[d]
0829_a	50182.71652	71686083	71688931	2848	soft	yes
0829_b	50182.78550	71691827	71695107	3280	soft	yes
0829_c	50182.85309	71697587	71701027	3440	soft	yes
0837a_a	50190.58735	72366723	72368371	1648	soft	no
0837a_b	50190.65800	72372739	72374563	1824	soft	yes
0837b_a	50190.71884	72378019	72379795	1776	soft	no
0837c_a	50190.77772	72383379	72384611	1232	soft	no
0840_a	50193.44735	72613923	72615379	1456	soft	no
0840_b	50193.51680	72619667	72621635	1968	soft	no
0840_c	50193.58513	72625427	72627683	2256	soft	no

Notes.
[a] Data reference name, using MET day (see footnote (c)).
[b] Modified Julian Date of exposure midpoint; MDJ = JD—2400000.5.
[c] Mission Elapsed Time (MET), here in integer seconds, is the time since 1994 January 1 0 hr (UTC). The truncated fraction is 0.374 s. *RXTE* Standard 2 data is collected during 16 s intervals of Spacecraft time (SCT), which is related by MET = SCT + 3.374.
[d] Indicates whether a good fit (i.e., a fit with $\chi^2_\nu < 2$) was achieved or not.

(This table is available in its entirety in machine-readable form.)

of gas through the disk. As the poloidal field builds, magnetic pressure can at some point balance the ram pressure of the accreting gas, halting the flow and producing a truncated inner disk. Originally proposed by Bisnovatyi-Kogan & Ruzmaikin (1974), this theory was refined by Narayan et al. (2003) and the effect in question is referred to as a MAD.

The presence of a global magnetic field was also invoked to explain the presence of X-ray QPOs in BHBs (Tagger & Pellat 1999; Varnière et al. 2012). Here, magnetized disks were investigated in a theoretical framework known as the Accretion-Ejection Instability (AEI). The degree of disk magnetization was later claimed to be the basis for the different X-ray states in BHBs (Tagger et al. 2004), including the "A, B, and C" states that form the basis for the fast variability cycles in GRS1915 (see end of Section 5 and also Varniere et al. 2011).

When accretion close to a black hole is disrupted by a MAD, it is suggested that matter flows inward in discrete blobs which travel much slower than the free-fall velocity. During this phase, a significant fraction of the rest mass energy of the gas is expected to be released as heat, radiation, and mechanical energy. Simulations have recently shown that MADs are also capable of producing jets efficient at extracting spin energy (>100% efficiency in ideal circumstances which in part requires $a_* > 0.9$, Tchekhovskoy et al. 2011; McKinney et al. 2012).

We note that, thus far, simulations of MADs have mostly treated accretion disks of substantial thickness, since a thick flow facilitates the trapping of magnetic field lines. They have also been concentrated on systems with low radiative energy loss. More study is needed to assess the importance of MADs in the thin-disk, high-spin regime with high radiative losses. We remind the reader that GRS1915 is a system that belongs to the latter regime, and therefore our suggestions should be taken with due caution.

Our results show that $R_{\rm in}$ increases systematically with increasing disk luminosity, and hence the estimated mass accretion rate through the disk. However, if the sampling of time-disparate points at a given disk luminosity suggest the same $R_{\rm in}$, then it would be reasonable to presume that MAD must reach an equilibrium at a given $\dot{M}$, i.e., that B-field losses (reconnection and outflows) must balance the continual inflow of field lines seeded by the global field, so as to hold $R_{\rm in}$ steady. In the MAD scenario, the $R_{\rm in}$–$\dot{M}$ correlation further suggests that the global B-field is not random, but is also regulated in some way by accretion, e.g., arising from some type of dynamo in the outer disk. If not, then changes in the global field strength would likely destroy the correlation, as we sampled dozens of re-formed hard-steady conditions during the 16 years of *RXTE* observations. Additional questions concern the details of magnetic flux accumulation and the effects of disk thickness. Further work is needed to consider these issues and properly assess MAD as an explanation for hard-steady conditions.

Varniere et al. (2011) present another method of classifying observations based on the type of instability that occurs in the disk. This was first developed as a continuation of the extended Magnetic Flood Scenario (Tagger et al. 2004; Varnière et al. 2007), which was proposed to explain the overall behavior of the source based on the stored magnetic flux in the inner region of the system. The classification is based on two key parameters: the degree of magnetization of the disk (β) and the position of the inner edge of the disk ($\xi_{\rm int}$). From these two parameters, they obtain four possible "states" harboring up to two simultaneous instabilities and having quite distinctive timing specificities. Their spectral differences have not been explored in detail, but an overall behavior can be deduced from the different instabilities.

The softer states are characterized by a lower magnetization level in the disk, while the harder states tend to have a fully magnetized disk. This clearly separates the behavior of both states, even though they can reach similar inner radii. Indeed in the soft, low-magnetization state, the instabilities that can occur, such as the magnetorotational instability (MRI; Balbus & Hawley 1991) and the Rossby Wave Instability (RWI; Tagger & Varnière 2006), both tend to heat up the disk more than the instabilities known to occur in a fully magnetized disk. Using the position of the inner edge of the disk, the four-state classification separates the softer states further. While the MRI can occur independently of the disk position, the RWI dominates when the inner edge of the disk gets closer to the last stable orbit. This will cause further heating of the inner region of the disk while maintaining a relatively stable inner edge. As a consequence of the low magnetization, the softer

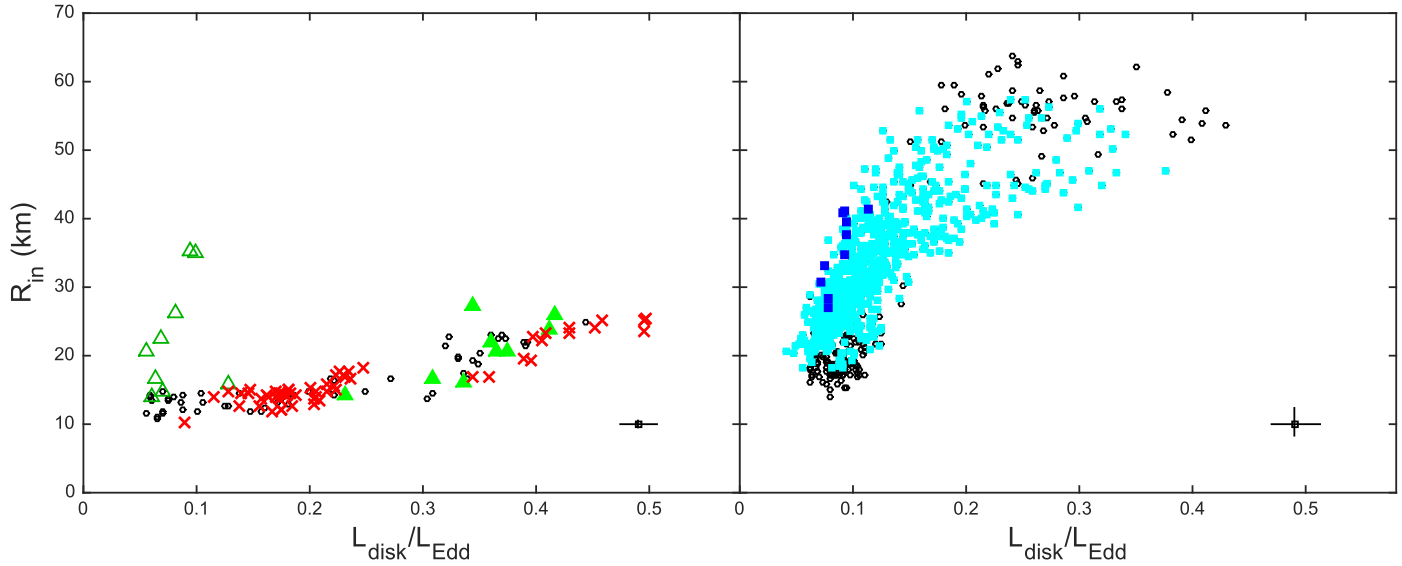

Figure 13. Left: steady-soft observations with those matching the thermal (red crosses) and SPL state (green triangles) criteria marked. Filled green triangles mark SPL state observations with LFQPOs while open green triangles mark those with no LFQPOs. Right: steady-hard observations with those matching the hard (dark blue filled squares) state criteria marked. Cyan squares show steady-hard data matching a relaxed definition of the hard state (see text for details). No steady-hard points matched the thermal or SPL state definitions and no steady-soft points matched the hard-state definition. Black open circles mark observations which do not fit within the state classifications.

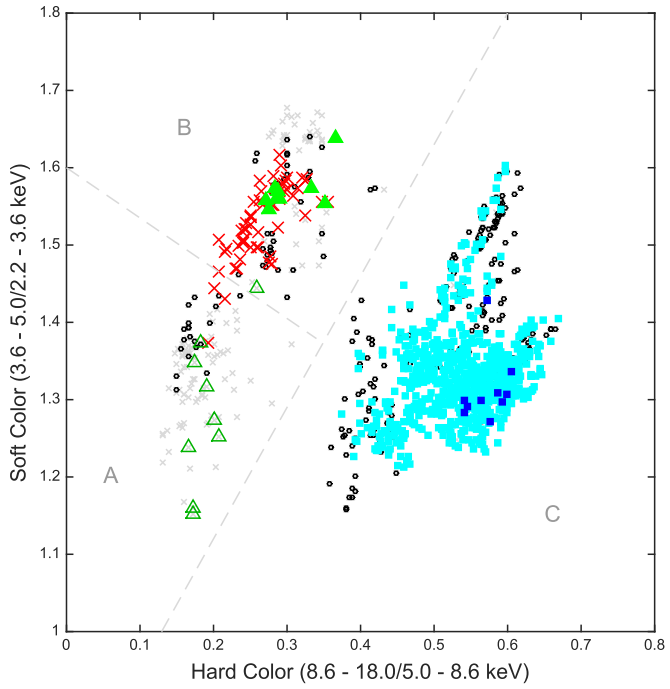

Figure 14. Normalized CD with symbols as defined in Figure 13. Light gray dashed lines roughly demarcate the regions "A, B, and C" regions that govern fast variability cycles in GRS1915 (see also Figure 8 in Belloni et al. 2000). State assignments appear to map to the A, B, and C regions. Light gray crosses indicate observations that did not satisfy the goodness-of-fit criterion.

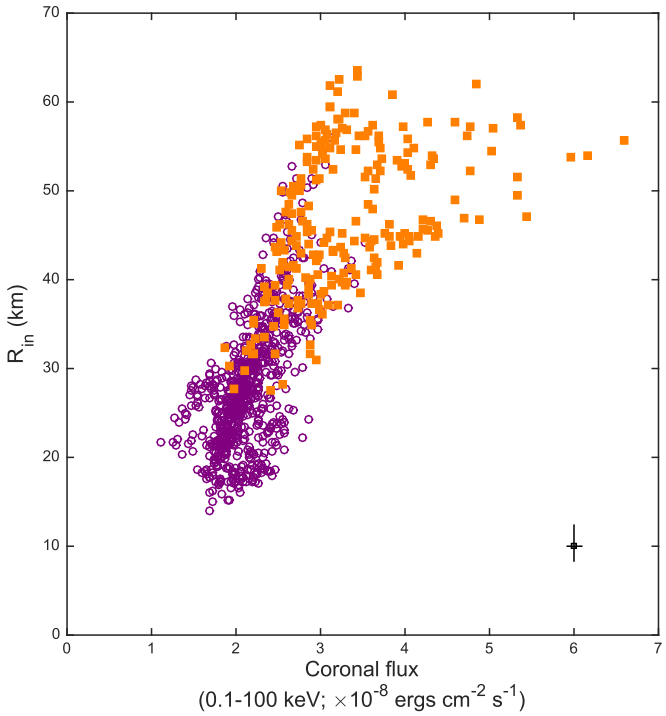

Figure 15. Observations with Type 1 (orange squares) and Type 2 (purple circles) LFQPOs represented in the plot of $R_{\rm in}$ vs. coronal flux. The types are defined within the text.

states will tend to have more limited coronal emission than the harder states. Using an approach similar to that of Varnière & Tagger (2002), we can also infer that the coronal emission will be higher when the RWI is active in the disk, i.e., when the inner edge of the disk is smaller.

Within this framework, the harder states tend to be explained as having a fully magnetized disk, and hence the AEI (Tagger & Pellat 1999) causes the transport of angular momentum and the LFQPO. In this scenario (Tagger et al. 2004; Varnière et al. 2007), the inner edge of the disk is pushed outward (as in MAD) because of the magnetic flux stored inside the inner region. As the stored magnetic flux is destroyed due to the magnetic flux being transported in by the accretion flow in the disk, the inner edge of the disk moves toward $R_{\rm ISCO}$. This process, depending on the magnetization of the disk, is slow enough for the state to be "steady" during one observation window. This process is also the origin

of the radio emission visible in those states. Once again, if the inner edge of the disk stays close to the last stable orbit, the RWI will simultaneously occur in the inner region, but this time, as shown in Varnière & Tagger (2002), the coronal emission will be higher when the disk is away from its last stable orbit.

While a one-on-one association with the different sub-branches of steady-hard and steady-soft is difficult, the level of magnetization in the disk may account for the behavioral differences we have observed.

6.4. The X-Ray–Radio Correlations of the G12-like and R10 Observations Within the Steady-hard

We find evidence of a (nonlinear) X-ray–radio correlation for GRS1915 that occurs during the decline into two luminosity dips in the steady-hard light curves (Figure 10). When examining the coronal parameters of these G12-like points, which are limited to the decline period, we find changes which suggest a move toward more canonical hard-state characteristics (Section 4.3). The changes are as follows. (1) While all steady-hard observations show significantly low values of $E_{\rm fold}$, these observations show an increase in $E_{\rm fold}$ that corresponds to a decrease in the curvature of the Compton component. This shows a move toward a less curved power law, typical of hard-state BHBs. (2) A majority of the steady-hard observations show $1.4 < \Gamma < 2.1$ with a mean value 1.69 ± 0.26, which is typical for a hard state. These specific observations occupy a compact spot in the middle of this range and show a much less variability ($\Gamma = 1.72 \pm 0.09$) suggesting a separate population with a more regular power-law index.

Our fit to the G12-like points matches the slope of the upper G12 track (Gallo et al. 2012, see also Gallo et al. 2003, 2006; Corbel et al. 2008), although we note that our uncertainty is large. The changes observed in the coronal parameters within the G12 points increase our confidence that they might map to one of the G12 tracks, which are defined using canonical hard state BHBs. Finally, the G12 points lie almost exactly on the upper G12 track (red line in Figure 9) leading us to believe that these might be one and the same.

Our fit to the R10 points obtained using isolated coronal flux (i.e., without the contribution of disk component) produces a log slope of $\eta \sim 1.12 \pm 0.13$, which is much lower than that observed by Rushton et al. (2010). We find that our value for the slope is consistent with the lower G12 track (blue line in Figure 9). The two slopes observed within the steady-hard observations of GRS1915 are reminiscent of the two slopes observed in the hard-state observations of H1743-322 (Coriat et al. 2011).

6.5. Effects Due to High Spin in the System

One of the most noticeable differences in GRS1915 when compared to canonical BHBs is the unusual curvature observed in the coronal component. Our analyses quantify this as $E_{\rm fold}$ values of $\sim$10 keV for the steady-soft observations and 10–30 keV for the majority of the steady-hard observations (see Figure 7(c)). This curvature has been a major source of difficulty in modeling the spectra of this system. We explained earlier, using the classical interpretation for Comptonization, that this curvature can be a result of a corona which is intensely cooled by the ample availability of soft photons from the hot inner disk. This leads us to the obvious next question: what causes the disk in GRS1915 to be so hot? The explanation seems to be high spin ($a_* \geqslant 0.98$; McClintock et al. 2006). The extreme spin, which allows the spacial dimension of $R_{\rm ISCO}$ to shrink down to limits smaller than for other known BHBs, could result in the production of a vast number of soft photons that can cool the corona intensely. This will lower the energy of the coronal electrons, inhibiting the upscatter of the soft photons to high enough energies to produce the usual power law observed in canonical BHBs.

7. SUMMARY

1. The steady state observations of GRS1915 naturally separate into two groups on the CD with a gap in the middle. We label these two groups steady-soft and steady-hard.
2. The spectral continuum of GRS1915 displays significant curvature of the Compton component ($E_{\rm fold} \sim 10$ keV for steady-soft and 10–30 keV for a majority of steady-hard), rendering commonly used models such as POWERLAW or SIMPL ineffective in representing the Comptonization. The new cutoff power-law model SIMPLCUT describes the curvature well. The extreme curvature suggests significant cooling of the corona in GRS1915.
3. The disk in GRS1915 is significantly hotter than canonical BHB disks. The temperatures of the disk in a majority of the steady-soft and steady-hard observations are $\sim$2 and $\sim$1.2 keV, respectively. Other BHBs show soft and hard observations with typical temperatures of $\leqslant$1 keV and $\leqslant$0.5 keV, respectively.
4. 96% of the steady-soft observations display an almost constant $R_{\rm in}$, which is usually observed in canonical soft-state observations of BHBs. However, 4% of the steady-soft observations show an increase in $R_{\rm in}$ at low X-ray luminosity.
5. The steady-hard observations exhibit the presence of a truncated disk with varying $R_{\rm in}$. The minimum $R_{\rm in}$ in the steady-hard observations agrees well with the $R_{\rm in}$ values for the steady-soft observations (and is therefore close to $R_{\rm ISCO}$), but increases by a factor of four at highest luminosity.
6. A strong correlation is noted between the disk and coronal flux in the steady-hard observations. The steady-soft observations show only a very weak correlation with comparatively less coronal flux, suggesting that the two coronae have different origins.
7. A sub-population within the steady-hard observations follows the upper G12 track during the luminosity decline period of two dips in the X-ray light curve ($50420 < {\rm MJD} < 50550$ and $53820 < {\rm MJD} < 53850$). GRS1915 shows a shift toward a canonical hard state when dropping down to these low luminosities.
8. The R10 observations display a slope that is consistent with the lower G12 track (0.98).
9. It has been shown earlier that the steady observations of GRS1915 yield spectra that resemble the thermal and hard states. We find evidence to suggest that all three states (thermal, SPL and hard) exists within the steady observations of GRS1915.
10. The locations of the thermal and SPL-qpo observations appear to correspond to the location of variable state B in the CD, while the location of the SPL-noqpo observations and the steady-hard observations may correspond to the

locations of A and C, respectively (Belloni et al. 2000). This suggests a link in the phenomenology of GRS1915 between short and long timescales.

We acknowledge the use of the Smithsonian Institution High Performance Cluster (SI/HPC) for spectral fitting. We also thank Jeff McClintock, Ramesh Narayan, Javier Garcia, and Malgosia Sobolewska for interesting and helpful discussions on the content of this paper. J.F.S. has been supported by NASA Einstein Fellowship grant PF5-160144. S.D.V. acknowledges partial support through a Smithsonian Institution CGPS grant. J.R. acknowledges financial support from the French Research National Agency: CHAOS project ANR-12-BS05-0009 (http://www.chaos-project.fr). P.V. and J.R. acknowledge financial support from the UnivEarthS Labex program at Sorbonne Paris Cité (ANR-10-LABX-0023 and ANR-11-IDEX-0005-02).

REFERENCES

Altamirano, D., Belloni, T., Linares, M., et al. 2011, ApJL, 742, L17
Arnaud, K. A. 1996, in ASP Conf. Ser. 101, Astronomical Data Analysis Software and Systems V, ed. G. H. Jacoby, & J. Barnes (San Francisco, CA: ASP), 17
Balbus, S. A., & Hawley, J. F. 1991, ApJ, 376, 214
Belloni, T., Klein-Wolt, M., Méndez, M., van der Klis, M., & van Paradijs, J. 2000, A&A, 355, 271
Belloni, T., Méndez, M., King, A. R., van der Klis, M., & van Paradijs, J. 1997a, ApJL, 488, L109
Belloni, T., Méndez, M., King, A. R., van der Klis, M., & van Paradijs, J. 1997b, ApJL, 479, L145
Belloni, T. M., Motta, S., & Casella, P. 2013, ATel, 5417, 1
Bisnovatyi-Kogan, G. S., & Ruzmaikin, A. A. 1974, Ap&SS, 28, 45
Brenneman, L. W., Madejski, G., Fuerst, F., et al. 2014, ApJ, 788, 61
Castro-Tirado, A. J., Brandt, S., & Lund, N. 1992, IAUC, 5590, 2
Corbel, S., Koerding, E., & Kaaret, P. 2008, MNRAS, 389, 1697
Corbel, S., Nowak, M. A., Fender, R. P., Tzioumis, A. K., & Markoff, S. 2003, A&A, 400, 1007
Coriat, M., Corbel, S., Prat, L., et al. 2011, MNRAS, 414, 677
Davis, S. W., Done, C., & Blaes, O. M. 2006, ApJ, 647, 525
Done, C., Gierliński, M., & Kubota, A. 2007, A&ARv, 15, 1
Ebisawa, K. 1991, PhD thesis, Univ. Tokyo
Ebisawa, K., Ogawa, M., Aoki, T., et al. 1994, PASJ, 46, 375
Esin, A. A., McClintock, J. E., & Narayan, R. 1997, ApJ, 489, 865
Fender, R., & Belloni, T. 2004, ARA&A, 42, 317
Fender, R. P., Garrington, S. T., McKay, D. J., et al. 1999b, MNRAS, 304, 865
Fender, R., Corbel, S., Tzioumis, T., et al. 1999a, ApJL, 519, L165
Frank, J., King, A., & Raine, D. 1992, Accretion Power in Astrophysics (Cambridge: Cambridge Univ. Press)
Gallo, E., Fender, R. P., Miller-Jones, J. C. A., et al. 2006, MNRAS, 370, 1351
Gallo, E., Fender, R. P., & Pooley, G. G. 2003, MNRAS, 344, 60
Gallo, E., Miller, B. P., & Fender, R. 2012, MNRAS, 423, 590
García, J. A., McClintock, J. E., Steiner, J. F., Remillard, R. A., & Grinberg, V. 2014, ApJ, 794, 73
Gierliński, M., & Done, C. 2004, MNRAS, 347, 885
Greiner, J., Cuby, J. G., McCaughrean, M. J., Castro-Tirado, A. J., & Mennickent, R. E. 2001, A&A, 373, L37
Grove, J. E., Johnson, W. N., Kroeger, R. A., et al. 1998, ApJ, 500, 899
Hannikainen, D. C., Rodriguez, J., Vilhu, O., et al. 2005, A&A, 435, 995
Hua, X.-M., & Titarchuk, L. 1995, ApJ, 449, 188
Jahoda, K., Markwardt, C. B., Radeva, Y., et al. 2006, ApJS, 163, 401
Kitamoto, S., Tsunemi, H., Pedersen, H., Ilovaisky, S. A., & van der Klis, M. 1990, ApJ, 361, 590
Klein-Wolt, M., Fender, R. P., Pooley, G. G., et al. 2002, MNRAS, 331, 745
Kolehmainen, M., & Done, C. 2010, MNRAS, 406, 2206
Kotani, T., Ebisawa, K., Dotani, T., et al. 2000, ApJ, 539, 413
Kubota, A., & Done, C. 2004, MNRAS, 353, 980
Laor, A. 1991, ApJ, 376, 90
Lee, J. C., Reynolds, C. S., Remillard, R., et al. 2002, ApJ, 567, 1102
Lin, D., Remillard, R. A., & Homan, J. 2007, ApJ, 667, 1073
Lin, D., Remillard, R. A., & Homan, J. 2009, ApJ, 696, 1257
Makishima, K., Maejima, Y., Mitsuda, K., et al. 1986, ApJ, 308, 635
Makishima, K., Takahashi, H., Yamada, S., et al. 2008, PASJ, 60, 585
McClintock, J. E., Narayan, R., & Steiner, J. F. 2014, SSRv, 183, 295
McClintock, J. E., & Remillard, R. A. 2006, in Black Hole Binaries, Compact Stellar X-Ray Sources, ed. W. H. G. Lewin, & M. van der Klis (Cambridge: Cambridge Univ. Press), 157
McClintock, J. E., Shafee, R., Narayan, R., et al. 2006, ApJ, 652, 518
McClintock, J. E., Haswell, C. A., Garcia, M. R., et al. 2001, ApJ, 555, 477
McKinney, J. C., Tchekhovskoy, A., & Blandford, R. D. 2012, MNRAS, 423, 3083
Middleton, M., Done, C., Gierliński, M., & Davis, S. W. 2006, MNRAS, 373, 1004
Miller, J. M., Homan, J., & Miniutti, G. 2006, ApJL, 652, L113
Miller, J. M., & Rykoff, E. 2007, ATel, 1066, 1
Mirabel, I. F., & Rodríguez, L. F. 1994, Natur, 371, 46
Mitsuda, K., Inoue, H., Koyama, K., et al. 1984, PASJ, 36, 741
Muno, M. P., Morgan, E. H., & Remillard, R. A. 1999, ApJ, 527, 321
Muno, M. P., Remillard, R. A., & Chakrabarty, D. 2002, ApJL, 568, L35
Muno, M. P., Remillard, R. A., Morgan, E. H., et al. 2001, ApJ, 556, 515
Narayan, R., Igumenshchev, I. V., & Abramowicz, M. A. 2003, PASJ, 55, L69
Neilsen, J., & Lee, J. C. 2009, Natur, 458, 481
Neilsen, J., Remillard, R. A., & Lee, J. C. 2011, ApJ, 737, 69
Pooley, G. G., & Fender, R. P. 1997, MNRAS, 292, 925
Poutanen, J. 1999, in Accretion Disc Corona Models and X/γ-ray Spectra of Accreting Black Holes, ed. M. A. Abramowicz, G. Björnsson, & J. E. Pringle (Cambridge: Cambridge Univ. Press), 100
Prat, L., Rodriguez, J., & Pooley, G. G. 2010, ApJ, 717, 1222
Reid, M. J., McClintock, J. E., Steiner, J. F., et al. 2014, ApJ, 796, 2
Remillard, R. A., & McClintock, J. E. 2006, ARA&A, 44, 49
Rodriguez, J., Shaw, S. E., Hannikainen, D. C., et al. 2008, ApJ, 675, 1449
Rushton, A., Spencer, R., Fender, R., & Pooley, G. 2010, A&A, 524, A29
Sądowski, A. 2009, ApJS, 183, 171
Sądowski, A., Abramowicz, M., Bursa, M., et al. 2011, A&A, 527, A17
Shafee, R., McClintock, J. E., Narayan, R., et al. 2006, ApJL, 636, L113
Shidatsu, M., Ueda, Y., Tazaki, F., et al. 2011, PASJ, 63, 785
Shimura, T., & Takahara, F. 1995, ApJ, 445, 780
Sobczak, G. J., McClintock, J. E., Remillard, R. A., et al. 2000, ApJ, 544, 993
Sobczak, G. J., McClintock, J. E., Remillard, R. A., Bailyn, C. D., & Orosz, J. A. 1999, ApJ, 520, 776
Steiner, J. F., McClintock, J. E., Orosz, J. A., et al. 2014, ApJ, 793, L29
Steiner, J. F., McClintock, J. E., & Reid, M. J. 2012, ApJL, 745, L7
Steiner, J. F., McClintock, J. E., Remillard, R. A., et al. 2010, ApJL, 718, L117
Steiner, J. F., McClintock, J. E., Remillard, R. A., Narayan, R., & Gou, L. 2009a, ApJL, 701, L83
Steiner, J. F., Narayan, R., McClintock, J. E., & Ebisawa, K. 2009b, PASP, 121, 1279
Steiner, J. F., Reis, R. C., McClintock, J. E., et al. 2011, MNRAS, 416, 941
Straub, O., Bursa, M., Sadowski, A., et al. 2011, A&A, 533, A67
Tagger, M., & Pellat, R. 1999, A&A, 349, 1003
Tagger, M., & Varnière, P. 2006, ApJ, 652, 1457
Tagger, M., Varnière, P., Rodriguez, J., & Pellat, R. 2004, ApJ, 607, 410
Takizawa, M. 1991, Master's thesis, MSc. thesis, Univ. Tokyo
Tanaka, Y., & Lewin, W. H. G. 1995, in X-ray Binaries, ed. W. Lewin, J. van Paradijs, & E. van den Heuvel (Cambridge: Cambridge Univ. Press), 126
Tchekhovskoy, A., Narayan, R., & McKinney, J. C. 2011, MNRAS, 418, L79
Terada, K., Kitamoto, S., Negoro, H., & Iga, S. 2002, PASJ, 54, 609
Titarchuk, L. 1994, ApJ, 434, 570
Titarchuk, L., & Lyubarskij, Y. 1995, ApJ, 450, 876
Titarchuk, L., & Seifina, E. 2009, ApJ, 706, 1463
Ueda, Y., Inoue, H., Tanaka, Y., et al. 1998, ApJ, 492, 782
Varnière, P., & Tagger, M. 2002, A&A, 394, 329
Varniere, P., Tagger, M., & Rodriguez, J. 2011, A&A, 525, A87
Varnière, P., Tagger, M., & Rodriguez, J. 2012, A&A, 545, A40
Varnière, P., Tagger, M., Rodriguez, J., & Cadolle Bel, M. 2007, in Proc. Annual Meeting of the French Society of Astronomy and Astrophysics, SF2A-2007, ed. J. Bouvier, A. Chalabaev, & C. Charbonnel, 221
Wilms, J., Allen, A., & McCray, R. 2000, ApJ, 542, 914
Wilson-Hodge, C. A., Cherry, M. L., Case, G. L., et al. 2011, ApJL, 727, L40
Zdziarski, A. A., Grove, J. E., Poutanen, J., Rao, A. R., & Vadawale, S. V. 2001, ApJL, 554, L45
Zimmerman, E. R., Narayan, R., McClintock, J. E., & Miller, J. M. 2005, ApJ, 618, 832